

**Department of Physics and Astronomy
University of Heidelberg**

Characterising candidate metal-poor stars
of the Hamburg/ESO Survey using Gaia DR2 data

Bachelor Thesis in Physics
submitted by

Jens Richter

born in Saarbrücken (Germany)

14.08.2020

This Bachelor Thesis has been carried out by Jens Richter at the
Zentrum für Astronomie der Universität Heidelberg, Landessternwarte
under the supervision of
Prof. Norbert Christlieb

Abstract

The investigation of metal-poor stars provides the opportunity to study a long list of topics, for example the nature of the first stars or the evolution of the Galaxy. Due to its spectral resolution, the Hamburg/ESO Survey (HES) is well-suited for automatic selection procedures of candidate metal-poor stars. In this thesis, candidate metal-poor stars of the HES are characterised. For this purpose, three samples were crossmatched to the Gaia DR2 catalogue, which provides precise astrometry and photometry for more than one billion stars. In the crossmatch procedure, which included a search radius of $3''$ and a plausibility check based on the photometry, $\sim 91\%$, $\sim 73\%$ and $\sim 98\%$ of stars in the three samples could be identified. From the first sample, a transformation between the Gaia colour $BP - RP$ and the Johnson-Cousins colour $B - V$ was determined. Colour-magnitude diagrams were produced, which were overplotted with stellar isochrones of different metallicities, from which the metallicities of the samples appear to be below $[Fe/H] = -2.0$. Objects in the white dwarf region as well as the region on the blue end of the largest sample were selected and some of their spectra investigated by eye. Of the selected stars, 16 hot subdwarfs and three white dwarfs could be found in the Simbad database; of the spectra investigated by eye, three likely belong to white dwarfs and one to a hot subdwarf, while most of the others belong to main sequence stars. Finally, for the effective temperature and surface gravity of the stars in the third sample, the systematic difference to these parameters derived from Gaia DR2 data was determined, finding an offset of (150 ± 7) K for the effective temperature and (0.45 ± 0.02) dex for the surface gravity.

Zusammenfassung

Die Untersuchung metallarmer Sterne ermöglicht das Studium vieler Themen, beispielsweise der Eigenschaften der ersten Sterne oder der Evolution der Galaxis. Aufgrund ihrer spektralen Auflösung eignet sich die Hamburg/ESO Survey (HES) gut für automatische Selektionsverfahren metallarmer Kandidatensterne. In dieser Arbeit werden metallarme Kandidatensterne der HES charakterisiert. Hierfür wurden drei Stichproben mit dem Gaia DR2 Katalog abgeglichen, der präzise Astrometrie und Photometrie für mehr als eine Milliarde Sterne bereitstellt. Durch die Crossmatch-Prozedur, die einen Suchradius von $3''$ sowie einen auf der Photometrie basierenden Plausibilitätscheck beinhaltet, konnten $\sim 91\%$, $\sim 73\%$ und $\sim 98\%$ der Sterne der drei Stichproben identifiziert werden. Mit der ersten Stichprobe wurde die Transformation zwischen der Gaia-Farbe $BP - RP$ und der Johnson-Cousins-Farbe $B - V$ bestimmt. Es wurden Farben-Helligkeits-Diagramme erstellt, in die Isochronen unterschiedlicher Metallizitäten geplottet wurden, denen zufolge die Metallizitäten der Stichprobe im Allgemeinen niedriger als $[Fe/H] = -2.0$ zu sein scheinen. Objekte im Bereich der weißen Zwerge sowie am blausten Ende der größten Stichprobe wurden selektiert und einige ihrer Spektren nach Augenmaß untersucht. Von den selektierten Sternen konnten 16 heiße Unterzwerge sowie drei weiße Zwerge in der Simbad-Datenbank identifiziert werden; von den nach Augenmaß untersuchten Spektren gehören drei wahrscheinlich zu weißen Zwergen, eins zu einem heißen Unterzerg, während die meisten anderen wahrscheinlich Hauptreihensternen zuzuordnen sind. Schließlich wurden für die effektive Temperatur und die Oberflächengravitation in der dritten Stichprobe die systematischen Unterschiede zu den aus Gaia-DR2-Daten abgeleiteten entsprechenden Parametern bestimmt, wobei ein Offset von (150 ± 7) K für die effektive Temperatur und (0.45 ± 0.02) dex für die Oberflächengravitation gefunden wurde.

Contents

1	Introduction	5
2	Observational techniques	7
2.1	Astrometry	7
2.2	Photometry	13
2.3	Spectroscopy	17
3	The Sample	21
3.1	The Hamburg/ESO Survey	21
3.2	Sample selection	23
4	Data analysis	26
4.1	Crossmatch	26
4.2	Colour-magnitude diagrams	29
4.3	Selection and follow-up spectra	33
4.4	Comparison of stellar parameters	36
4.4.1	Effective temperature	36
4.4.2	Surface gravity	38
5	Results and conclusions	42
6	Outlook	44
A	Appendix	47

List of Figures

1	Flux map of the Milky Way	7
2	Content of Gaia DR2	8
3	Scanning law of Gaia	9
4	Exploded view of the Gaia satellite	9
5	The payload module	10
6	Focal plane assembly	11
7	Distribution of Gaia positional errors in the Galaxy	11
8	Uncertainties of Gaia positions and parallaxes	12
9	Gaia DR2 magnitude distribution	12
10	UBVRI passbands	14
11	Charge transfer within a CCD	15
12	Gaia passbands	16
13	Échelle spectrum of the Sun	17
14	Comparison between low- and high-resolution spectrum	18
15	Optical layout of basic slit spectrometer	19
16	Reflection grating and grating equation	20
17	Layout of EMMI	20
18	HES survey area	21
19	HES example spectra	22
20	Calibrations of colour and line index	23
21	Cutoff line for metal-poor candidate sample	24
22	Distribution of metallicities in the HERES sample	25
23	Statistical distribution of colours	27
24	Angular distance between objects and matched objects	27
25	Distribution of proper motions	28
26	Proper motion multiplied by epoch difference	28
27	Transformation curves between $BP - RP$ and $B - V$	29
28	CMDs before dereddening	30
29	Dereddened CMD of the first sample	31
30	CMDs of the first sample including isochrones	31
31	CMDs of the second sample including isochrones	32
32	Kiel diagram and CMD of the third sample	32
33	Cutoff line applied to the first sample	33
34	Hot subdwarfs and white dwarfs from SIMBAD	35
35	Comparison of effective temperatures	36
36	Linear fits between the temperatures	37
37	Residual plot of temperatures including offset line	37
38	Comparison of temperatures using the benchmark stars	38
39	Isochrone in CMD for mass determination	39
40	Comparison of surface gravities	40
41	Linear fits between surface gravities	41

List of Tables

1	Coefficients for extinction A_G	30
2	White dwarfs found in SIMBAD	34
3	Hot subdwarfs found in SIMBAD	34

1 Introduction

During the latter half of the past century, the gradual recognition of the diversity of chemical abundance patterns across stars in the Galaxy paved the way for the exploration of a number of issues by means of investigation of, in particular, metal-poor stars. The assumption that the metallicity is representative of a star's age (with the most metal-poor stars being the oldest), alongside the theoretically motivated supposition that stars and galaxies started forming 100-200 Myr after the Big Bang, allows for the examination of the conditions in the early Universe, using the chemical abundances of stars (Frebel & Norris 2015). However, since individual stars have to be observed in great detail, this examination is restricted to the Milky Way and its dwarf galaxy satellites (as reflected by the term “near-field cosmology” used by Freeman & Bland-Hawthorn 2002).

Within the field of research known as *Stellar archaeology*, much effort has been put into the search for extremely metal-poor stars ($[\text{Fe}/\text{H}] < -3.0$) in the Galactic halo, as they purvey the means to investigate a long list of topics. Beers & Christlieb (2005) name and discuss several of them, including the nature of the Big Bang by comparing the amount of lithium from Big Bang models to the abundance in very metal-poor stars, the nature of the first stars (see Bromm & Larson 2004), the first mass function (which is of major relevance for the evolution of galaxies and not to be equated to the initial mass function), predictions of element production by supernovae (since metal-poor stars are not contaminated by elements from several previous generations of stars), the nature of the metallicity distribution function of the galactic halo, and the astrophysical site(s) of neutron-capture element production by comparing the abundances of heavy elements in very metal-poor stars to theoretical predictions. Further related topics are early metal- and gas-mixing processes, galaxy formation and nucleosynthesis in general (Frebel & Norris 2015).

The chemical composition of a star's atmosphere indicates the time period in which it formed, since hints about the physical and chemical conditions of gas clouds are conserved in the stars which these gas clouds form. This means that the “amount of elements heavier than lithium in a star reflects the extent of chemical enrichment within its natal cloud” (Frebel & Norris 2015, pg. 632). However, this does not hold true for all stars: metal-poor post-asymptotic giant branch stars for example are assumed not to preserve the aforementioned hints due to mixing processes (see, e.g., Herwig 2005).

Another aspect to be considered when determining chemical abundances is the modelling of stellar atmospheres. Models of stellar atmospheres are primarily parameterised by the effective temperature T_{eff} , the surface gravity $\log g$ and the chemical composition $[\text{M}/\text{H}]$, where M denotes metals. Historically, one-dimensional (1D) models under the assumption of hydrostatic equilibrium, flux constancy and local thermodynamic equilibrium (LTE) were often used. Non-LTE (NLTE) formalisms and three-dimensional (3D) models provide data which comes closer to the real world, and although the implementation of such models is much more complex, 3D/NLTE models are increasing in popularity. Frebel & Norris (2013) consider the abundance differences between the results of the different models and recommend the 3D/NLTE abundance whenever possible, as they present more accurate results. However, most data to be used comes from 1D/LTE analyses (owing to their simplicity compared to 3D/NLTE analyses) and it is discouraged to mix data from the two models.

In this thesis, samples of metal-poor candidate stars are characterised. The visualisation of the samples in a colour-magnitude diagram (CMD) reveals how many objects are located in the different regions of the CMD, thus indicating which types of objects make up the samples. This allows for the selection of objects that are candidates for being of a certain type, as is done in this thesis for the white dwarf and hot subdwarf region, where a number of such objects are identified. Using stellar isochrones of different metallicities also gives a rough idea of the typical metallicities found in the samples.

Since models used to determine the metallicity of a star have to take their effective temperature and surface gravity into account, the precise knowledge of these parameters, or at least their uncertainties and deviations, is important. For one sample, the offsets of the effective temperatures and surface gravities between the values published in the sample and the values according to Gaia DR2 data are determined, thus providing an estimate of systematic deviations to be considered.

Definitions

Before proceeding, it is important to define some expressions which will be used throughout this thesis. The term *metal* refers to all elements in the periodic table heavier than helium. The *abundance* $\log \epsilon(A)$ of an element A is expressed in logarithmic form and relative to the hydrogen abundance. Specifically, if N_A and N_H are the number densities of atoms of A and H,

$$\log_{10} \epsilon(A) = \log_{10}(N_A/N_H) + 12. \quad (1)$$

Usually, stellar abundances are put into relation to the abundances of the Sun. For two elements A and B,

$$[A/B] = \log_{10}(N_A/N_B)_\star - \log_{10}(N_A/N_B)_\odot. \quad (2)$$

In particular, for hydrogen this is

$$[A/H] = \log_{10}(N_A/N_H)_\star - \log_{10}(N_A/N_H)_\odot. \quad (3)$$

The terms *underabundant* and *overabundant* are used if $[A/B] < 0$ and $[A/B] > 0$, respectively.

Typically, the iron abundance $[\text{Fe}/\text{H}]$ is measured to estimate the *metallicity* (which is the amount of metal within the star), as it is among the most abundant elements in stellar spectra. However, this equivalence seems to hold true only for $[\text{Fe}/\text{H}] > -4.0$: many stars with $[\text{Fe}/\text{H}] < -4.0$ exhibit large overabundances of carbon, nitrogen, oxygen as well as other elements relative to iron. To avoid vague expressions when discussing stars of different metallicities, the nomenclature of Beers & Christlieb (2005) is adopted (see their Table 1); notably, *extremely metal-poor* stars are defined by having an iron abundance of $[\text{Fe}/\text{H}] < -3.0$.

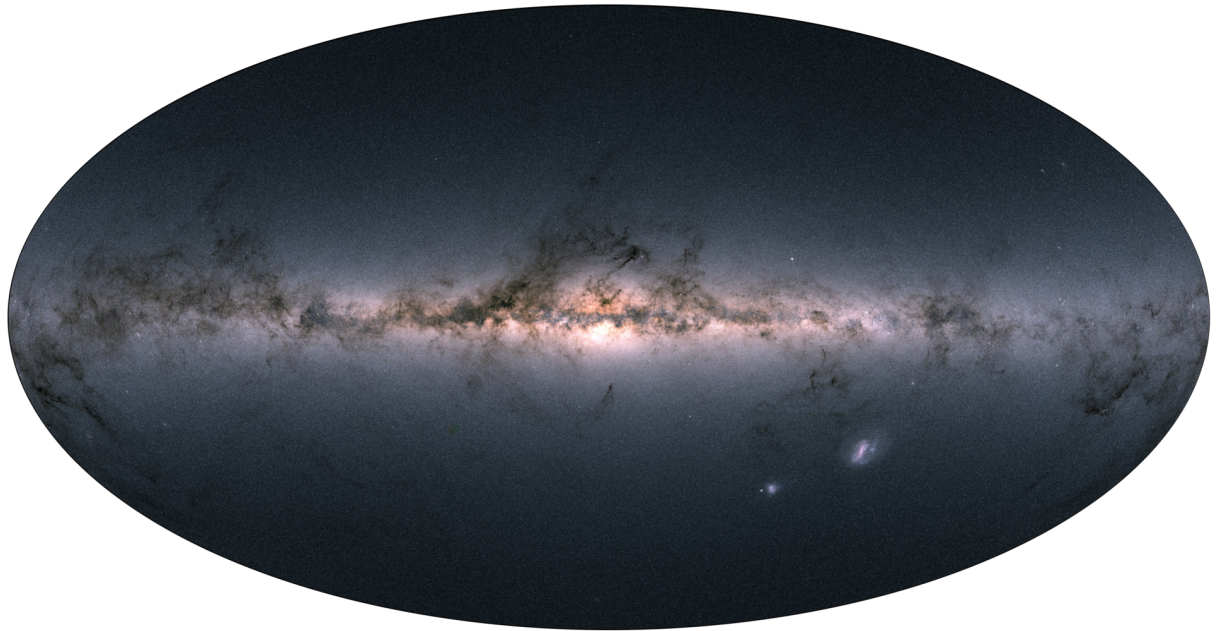


Figure 1: Image of the Milky Way in colour: map of the integrated fluxes observed in Gaia’s three passbands (Gaia Collaboration, Brown et al. 2018).

2 Observational techniques

2.1 Astrometry

Astrometry, sometimes labelled *positional astronomy*, is the “application of certain techniques, which one may call astrometric techniques, to determine the geometric, kinematic, and dynamic properties of the celestial bodies in our Universe” (Kovalevsky 2002, pg. 2). Specifically, the aim is to compile star catalogues which list the position, parallax and proper motion of objects within an according reference frame. These objects can be solar system objects, extragalactic objects such as quasars and distant galaxies, or stars. Constructing a reference frame in which the aforementioned quantities are given is another task of astrometry, for which quasars and distant galaxies are well-suited.

Throughout most of history, astronomy as a whole was mostly tantamount to astrometry. Beginning in ancient times, movements and positions of stars were used to devise calendars, predict eclipses, navigate at sea and at some point, catalogues of observations were introduced. Ptolemy’s star catalogue dating to AD 150 is the oldest surviving catalogue (Perryman 2012). Throughout the centuries, observations could be carried out with increasing precision, owing to the development of instruments such as the sextant and the telescope. During the past few decades, application of new technologies such as optical interferometers or charge coupled device (CCD) detectors greatly improved the accuracy of the observations, with recent observations (e.g. the Gaia survey) having accuracies in the microarcsecond range (Kovalevsky & Seidelmann 2004).

Carrying out astrometry from space was another important step towards high-precision measurements, with Hipparcos, the first satellite designed for that task, launching in 1989. By observing from space, several effects putting limitations on ground-based observations are avoided, e.g. atmospheric turbulence, which continually changes the apparent direction of the source, atmospheric refraction, which causes a systematic shift in apparent direction of the source and the movement of ground-based instruments with the rotating Earth, to name a few (Kovalevsky 2002).

Astrometry is essential for all other areas of astronomy, as the accurate pointing of telescopes on specific targets requires knowledge of their positions at that point in time. Astrometric data also allows for the derivation of the dynamics of gravitationally bound objects, distances of stars, masses of double or even multiple star systems and much more (Kovalevsky & Seidelmann 2004).

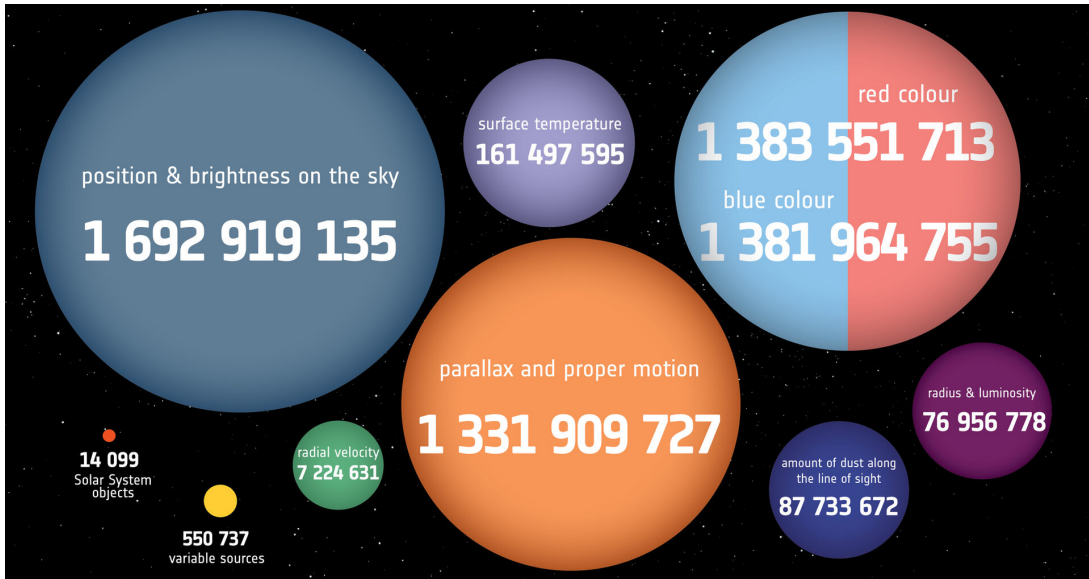


Figure 2: Content of the Gaia DR2 catalogue (Credit: ESA).

The Gaia mission

The main objective of the ESA Gaia mission is an astrometric and spectrophotometric survey of more than a billion celestial objects, including half a million quasars, a few hundred thousand asteroids, as well as a few million galaxies, down to 20th magnitude (Lindegren 2010, Figure 2). The original proposal, which suggested interferometry-based observations (GAIA=Global Astrometric Interferometer for Astrophysics), was submitted by Lennart Lindegren to ESA in 1993 as the successor to the Hipparcos mission. ESA approved the Gaia mission in 2000, although interferometry was abandoned in favour of direct imaging on CCDs (Høg 2014). The implementation phase started in 2006, with the Gaia spacecraft launching in December 2013 and the science operations phase beginning in the summer of 2014. The Gaia survey does not use an input catalogue in order for the survey to be unbiased and instead has two rows of 7 + 7 CCDs dedicated to first detecting objects (Sky Mapper SM1 & SM2), based on which observation windows are appointed to detected objects. The Data Processing and Analysis Consortium (DPAC) is responsible for the complex processing and analysis of mission data (Gaia Collaboration, Prusti et al. 2016).

Since global astrometry must be conducted from space in order to be accurate on a microarcsecond scale, the study of a large variety of scientific topics benefits greatly from Gaia data, as outlined by Perryman et al. (2001). The three-dimensional spatial and velocity distributions of stars as well as some of their astrophysical properties (e.g. surface gravity, effective temperature) obtained by Gaia are crucial for the understanding of the structure, history and future of our Galaxy.

The Gaia spacecraft and scanning space astrometry

The Gaia spacecraft is located at the second Lagrange point (L_2) of the Sun-Earth-Moon system, approximately 1.5 million kilometres from Earth, where it moves around L_2 in a Lissajous orbit, as the thermal conditions and radiation environment are preferable to those encountered in an Earth-bound orbit. The scanning law, which is the orientation of the spacecraft as a function of time, should maximise the uniformity of the sky coverage. It is defined by the spin rate around its spin axis of $\omega = 60'' \text{ s}^{-1}$, the solar-aspect angle (the angle between the Sun and the spin axis) of $\xi = 45^\circ$ and the precession of the spin axis with a precession period of 63 days (see Figure 3). The spin rate ω was chosen to adjust the speed of the images on the detector surface to the speed of the electrons inside the CCD, while the solar-aspect angle is 45° for maximum parallax sensitivity without the Sun, Earth or Moon entering the field of view of the telescopes. The speed of the precession should be as small as possible, but still fast enough for two consecutive loops to overlap, which is how the precession rate of $K = 5.8$ loops per year (corresponding to a precession period of 63 days) was selected (Gaia Collaboration, Prusti et al. 2016).

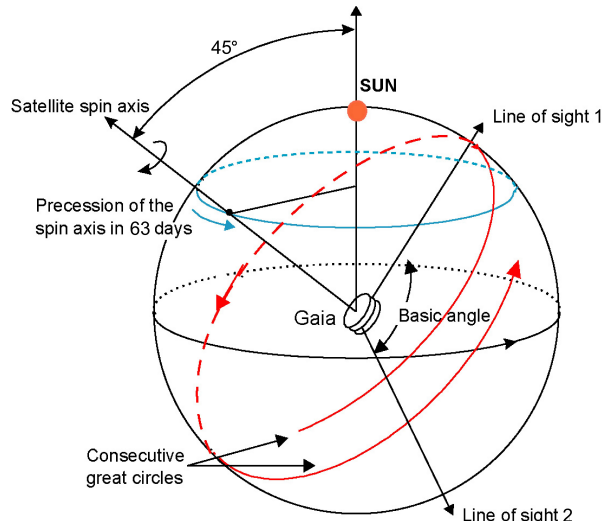


Figure 3: Visualisation of scanning law (Gaia Collaboration, Prusti et al. 2016).

Gaia uses *scanning space astrometry* to carry out its astrometric measurements: positional information is converted into timing data. Specifically, the measurement of the exact time at which the centre of a star image is at a certain position on the CCD pixel layout (*observation time*) provides the one-dimensional along-scan (AL) position of the star with respect to, i.e., the instrument axes. The simultaneously measured position in across-scan (AC) direction has, in comparison, a much lower precision in the case of Gaia; however, almost only AL measurements matter, so this is not problematic. Combining the direction in which the spacecraft points over time (*attitude*) as well as the mapping of the pixels in the detectors through the telescope onto the celestial sphere with the collected observation times allows for the assembly of the astrometric catalogue. A more in-depth characterisation of this method and its implementation in Gaia can be found in Lindegren & Bastian (2010).

In Figure 4, a schematic view of the Gaia spacecraft is given. (a) depicts the thermal tent shielding the payload module from the environment and from micro-meteoroid impacts, (b) shows the payload module, which is shown in greater detail in Figure 5 and further described in the following paragraphs, (c) portrays the structure of the service module, which supports the payload module mechanically and electronically, (d) depicts the propellant system, (e) the phased-array antenna for data transmission to Earth, and in (f) the deployable sunshield, which shields the payload

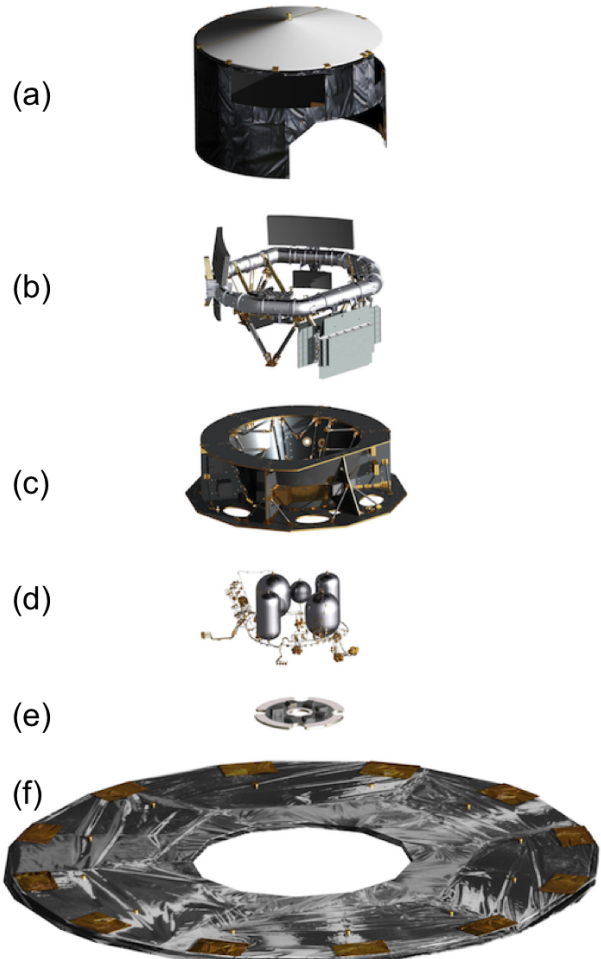


Figure 4: Exploded view of the Gaia satellite (Gaia Collaboration, Prusti et al. 2016); for details see text.

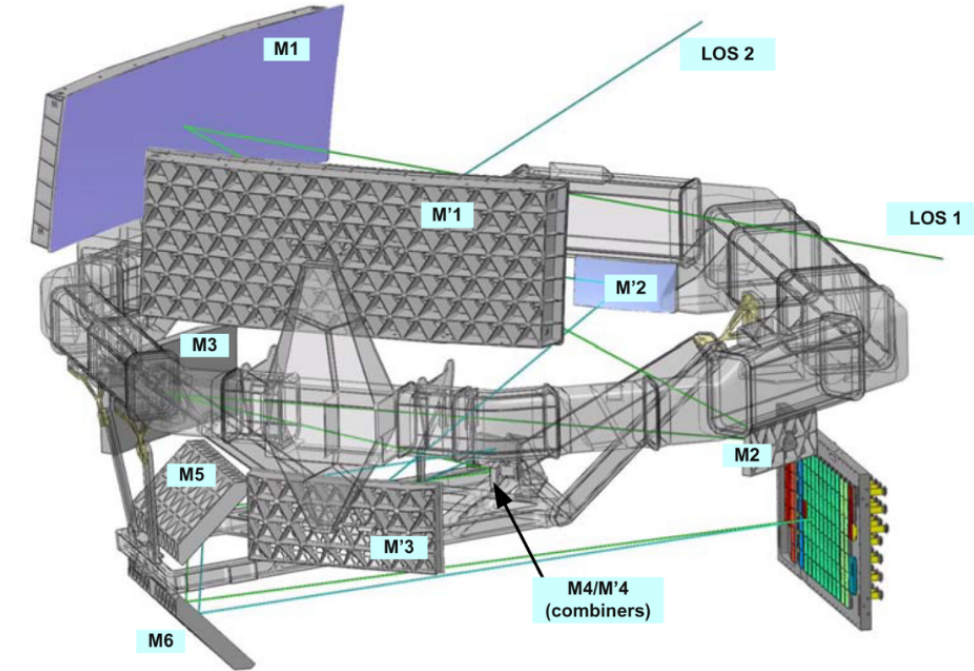


Figure 5: The payload module (Holl 2012).

from the Sun, is shown (Gaia Collaboration, Prusti et al. 2016).

As illustrated in Figure 5, the mirrors and focal plane assembly are attached to an optical bench and the complete payload module is placed above the service module. Beams coming from two identical, three-mirror anastigmatic telescopes with apertures of $1.45 \text{ m} \times 0.50 \text{ m}$, whose lines of sight are $\Gamma = 106.5^\circ$ apart, are guided into a common path by mirrors $M4/M'4$. Taking into account the focal length of 35 m, the beams are folded twice using additional reflectors ($M5, M6$) before finally reaching the focal plane assembly. Alignment and focussing mechanisms are built into the secondary mirrors ($M2/M'2$). The main concern when choosing the basic angle Γ , as discussed in Lindegren & Bastian (2010), was that $\Gamma = 360^\circ \cdot \frac{m}{n}$ is a bad choice for small integers m and n (see their Figure 3). Since for $\Gamma = 106.5^\circ$ $m = 71$ and $n = 240$, there is no problem.

The focal plane assembly (Figure 6) consists of 106 CCD detectors with 938 million pixels in total, which are cooled down to 163 K to minimise dark current and charge-transfer inefficiency arising from defect centres in the silicon lattice. There are three types of CCDs, indicated by their colour in Figure 6: the default broadband CCD (covering a broad bandpass), the blue-enhanced CCD (for short wavelengths) and the red-enhanced CCD (for long wavelengths). Each individual CCD contains 4500 along-scan and 1966 across-scan pixels and has its own proximity-electronics module (PEM) to adjust CCD operating points and to acquire the data. All CCD-PEM pairs of a row of CCDs are connected to one video processing unit (VPU), which collects the data and transfers it to the onboard storage. Since the complete data rate from all CCDs is too large for transmission to Earth, onboard reduction processes are implemented.

The astrometric measurements are carried out by the $7 + 7$ Sky Mapper CCDs (SM1 & SM2), which first detect objects, and the area of 62 CCDs labelled AF (astrometric field). Aside from AF1 and stars brighter than 13 mag, the data taken with the AF CCDs is binned in the AC direction over 12 pixels. The maximum object density of the instrument is about 1 050 000 objects per square degree, beyond that only the brightest sources are detected. The other CCDs on the focal plane are: two wave-front sensors of Shack-Hartmann type (WFS1/WFS2), a basic angle monitor (BAM) which monitors changes in the line of sight of the telescopes, 7 blue and 7 red CCDs (BP & RP) for photometry and 12 red CCDs for spectroscopy of bright stars (RVS) (Gaia Collaboration, Prusti et al. 2016).

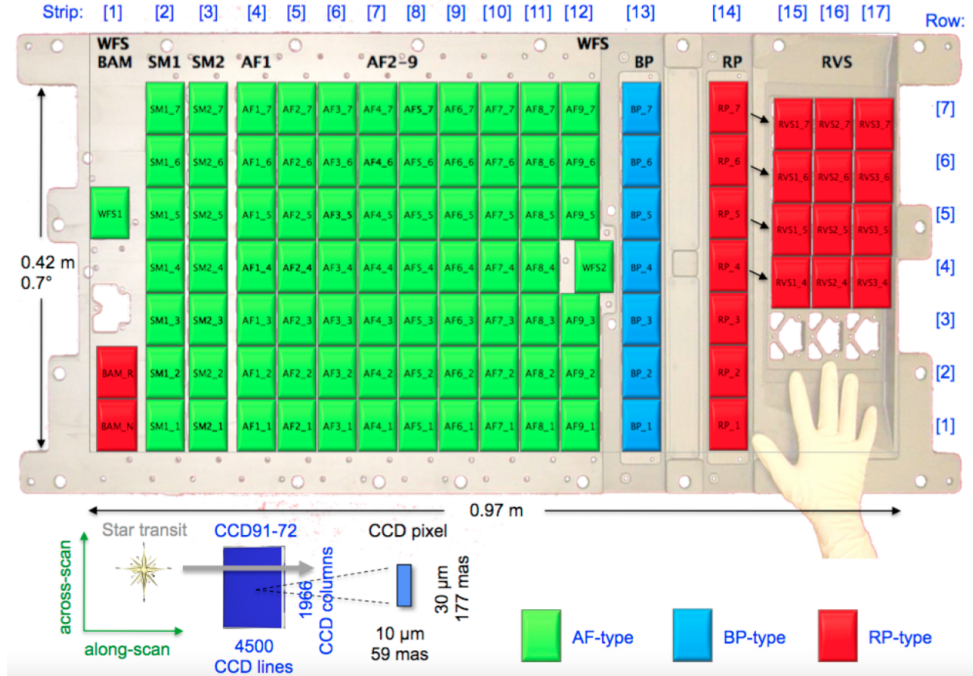


Figure 6: Focal plane assembly (Gaia Collaboration, Prusti et al. 2016).

Gaia Data Release 2

The second Gaia data release (Gaia DR2) catalogues almost 1.7 billion sources (see Figure 2), providing the position and apparent brightness of about 1693 million objects, 1332 million of which also come with parallaxes and proper motions. Furthermore, colour information is available for approximately 1.4 billion sources and radial velocities for about 7 million sources are given. Several astrophysical parameters have also been determined for a fraction of all sources: effective temperature for about 161 million sources, extinction for about 88 million sources, and radius and luminosity for about 77 million sources. Also included are 14099 solar system objects. Gaia Collaboration, Brown et al. (2018) summarise the contents of Gaia DR2.

Figure 7 shows how the positional uncertainties vary for objects across the Galaxy, where large scale structures, mostly arising from the scanning law, can be seen. Notably, the positions near the centre of the Galaxy are the least accurate (Gaia DR2 Documentation 12.4). The uncertainty in position and parallax as a function of the apparent

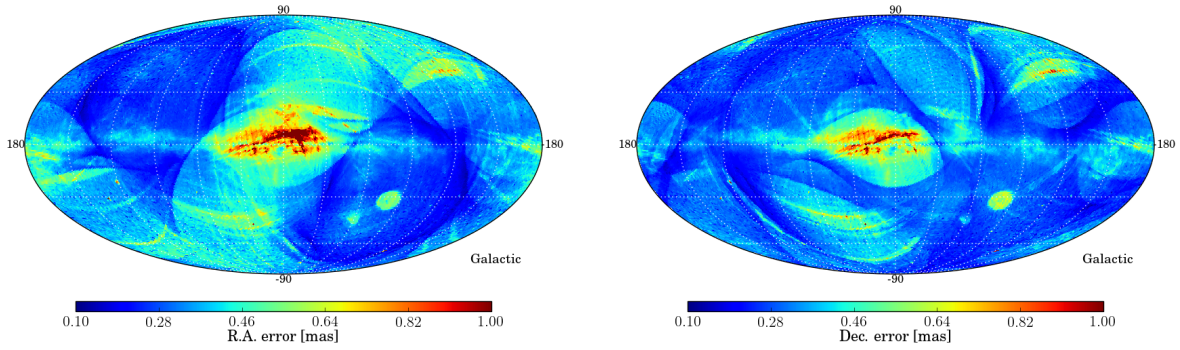


Figure 7: The distribution of positional errors in the Galaxy (Gaia DR2 Documentation 12.4).

magnitude G is visualised in Figure 8. As shown, the uncertainty of position and parallax is generally on the order of 0.04 mas at $G < 14$ mag, 0.1 mas for $G = 17$ mag and 0.7 mas for $G = 20$ mag. For the proper motion, the orders of uncertainty are 0.05 mas per year at $G < 14$ mag, 0.2 mas per year at $G = 17$ mag and 1.2 mas per year at $G = 20$ mag (Lindegren et al. 2018).

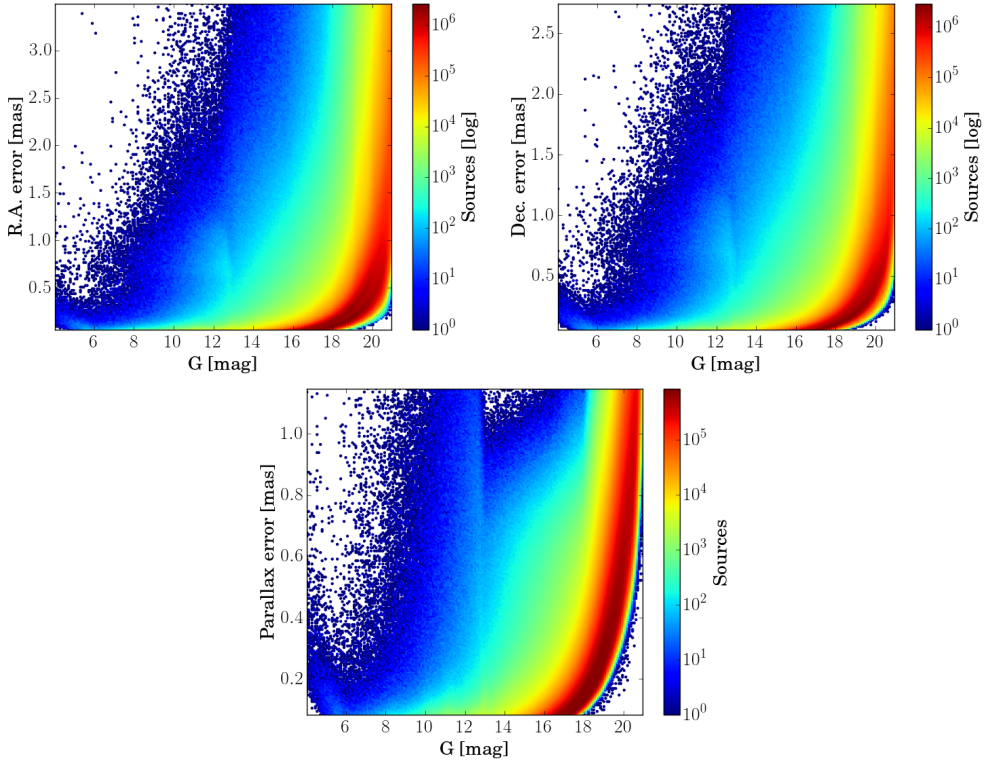


Figure 8: Uncertainties in position and parallax (Gaia DR2 Documentation 12.4 & 12.5).

The number of sources observed at different magnitudes is depicted in Figure 9, where 5-parameter astrometry refers to the sources for which position, parallax and proper motion could be determined, while 2-parameter astrometry refers to those sources for which only the position is available. From the curves, Gaia's limiting magnitude of about $G \simeq 21$ can be recognised (Gaia Collaboration, Brown et al. 2018).

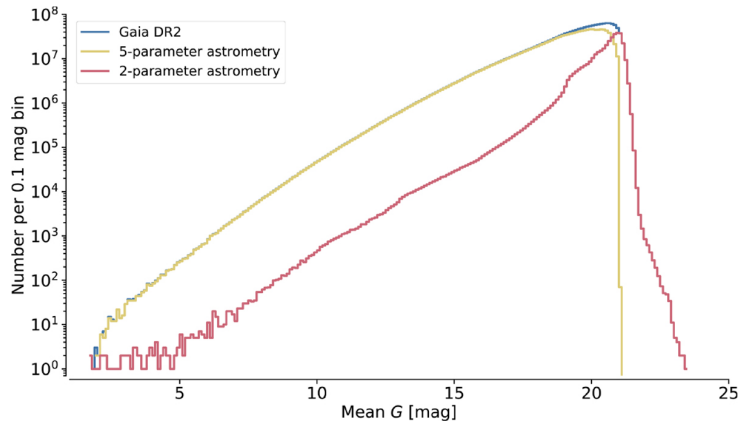


Figure 9: Gaia DR2 magnitude distribution (Gaia Collaboration, Brown et al. 2018).

2.2 Photometry

Photometry is the observation of a part of the spectral energy distribution of a star, where the wavelength range that is observed is given by the filters that are used. The brightness of an object, which is quantified as the *apparent magnitude* m , depends chiefly on the flux f_λ radiating from the object that reaches Earth and the so-called *sensitivity function* $E(\lambda)$ accounting for the transmissibility and efficiency of the optical system and detectors as well as, for ground-based observations, the transmissibility of the Earth's atmosphere (Casagrande & VandenBerg 2014). More precisely, if a star of radius R at a distance d from Earth has a flux of \mathcal{F}_λ at its photosphere, the flux f_λ outside the Earth's atmosphere (disregarding interstellar extinction) is given by

$$f_\lambda = \pi \frac{R^2}{d^2} \mathcal{F}_\lambda. \quad (4)$$

Due to absorption lines in the spectra, the measured flux will be lower than the flux for the continuous spectrum between lines. If the fraction of the flux absorbed by the lines is η_λ , the flux of the continuum \mathcal{F}_λ^c is related to \mathcal{F}_λ by

$$\pi \mathcal{F}_\lambda = \pi \mathcal{F}_\lambda^c (1 - \eta_\lambda). \quad (5)$$

The apparent magnitude m will be proportional to the integral

$$\frac{R^2}{d^2} \int_0^\infty \pi \mathcal{F}_\lambda E(\lambda) d\lambda \quad (6)$$

(Unsöld 1974) and is set to

$$\begin{aligned} m &= -2.5 \log \left(\frac{R^2}{d^2} \int_0^\infty \pi \mathcal{F}_\lambda E(\lambda) d\lambda \right) + \text{const.} \\ &= -2.5 \log \left(\int_0^\infty f_\lambda E(\lambda) d\lambda \right) + \text{const..} \end{aligned} \quad (7)$$

The logarithmic scale with factor 2.5 is motivated historically: with the above definition, the difference in magnitude for two stars with fluxes $f_{\lambda,1}$ and $f_{\lambda,2}$ is simply

$$m_1 - m_2 = -2.5 \log \left(\frac{f_{\lambda,1}}{f_{\lambda,2}} \right), \quad (8)$$

which means a star five magnitudes brighter than another star has 100 times the flux f_λ (Budding & Demircan 2007). In order to obtain a measure for a star's brightness, the *absolute magnitude* M of a star is defined as the apparent magnitude it would have at a distance of 10 pc. Using equation (7), the apparent and absolute magnitudes are connected via

$$m - M = 5 \log(d) - 5, \quad (9)$$

where d is the distance of the star in parsec and interstellar extinction is disregarded (Budding & Demircan 2007). If the interstellar extinction over distance d is A , this becomes

$$m - M = 5 \log(d) - 5 + A. \quad (10)$$

If the sensitivity function $E(\lambda)$ is left out of equation (7), the result is the *bolometric magnitude* m_{bol} , which takes into account radiation of all wavelengths, not just of the range given by $E(\lambda)$. In this context, the *bolometric correction* BC is defined as the difference between the bolometric magnitude m_{bol} and the visual magnitude m_{vis}

$$BC = m_{\text{bol}} - m_{\text{vis}}. \quad (11)$$

Two other parameters directly related to the flux F of a star are its *effective temperature* T_{eff} and its *luminosity* L , defined by

$$\pi F = \sigma T_{\text{eff}}^4 \quad \text{and} \quad (12)$$

$$L = 4\pi R^2 \cdot \pi F, \quad (13)$$

which are fundamental quantities of stars. Plotting the luminosity against the effective temperature for a number of stars yields the so-called *Hertzsprung-Russell diagram* (HRD). The position of a star within this diagram not only

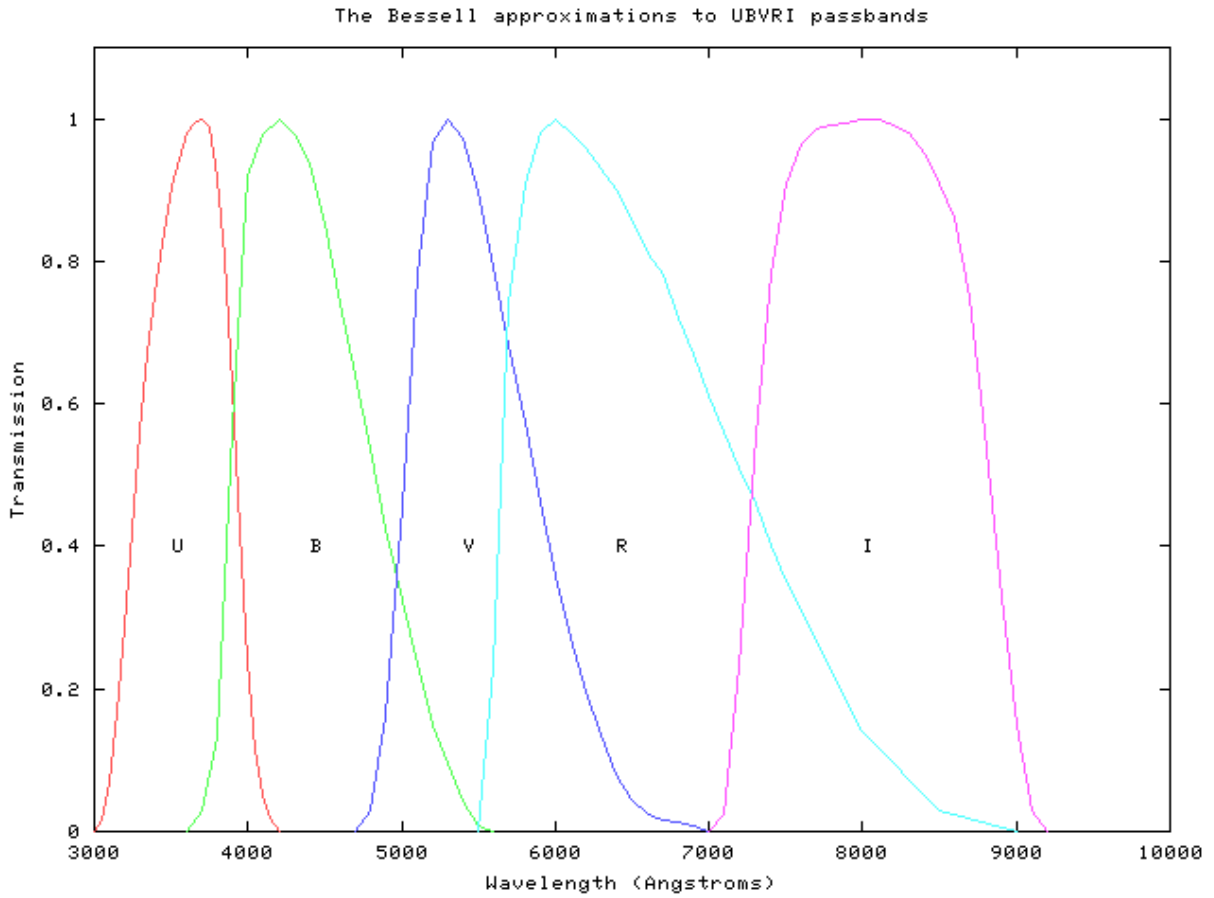


Figure 10: UBVRI passbands (Bessell 1990).

relates to its spectral type, but also provides information on the evolutionary status of the star, among other things (Unsöld 1974).

Photometric systems are characterised by the passbands they use, which determine the wavelength range that is detected. An early system upon which most other broad-band systems are based and which is still widely used is the so-called *UBV* system (Bessell 2005). The apparent magnitudes $U = m_U$, $B = m_B$ and $V = m_V$, measured using the corresponding bands and then equation (7), are calibrated by demanding that $U = B = V$ is fulfilled for A0V stars. Usually, Vega is used as the reference star for calibration (Unsöld 1974). The *UBV* system was expanded by Cousins, adding R and I passbands in the red and infrared region. This system is referred to as the Johnson-Cousins system (Bessell 2005). The passbands are shown in Figure 10.

Since different passbands cover different wavelengths ranges, the difference between two magnitudes, e.g. $B - V$ or $U - B$, is linked to the energy distribution in the spectrum of stars (Unsöld 1974). This difference is called *colour index* and for low values, the stars are labelled *blue*, while for higher values, they are labelled *red*. Due to blue light being scattered and absorbed in the interstellar dust to a higher degree than red light, a reddening of the measured spectra occurs and the colour index observed differs from the true colour index. This defines the so-called *colour excess* or *reddening*, e.g. for $B - V$

$$E(B - V) = (B - V) - (B - V)_0, \quad (14)$$

where $(B - V)$ is the measured colour index, and $(B - V)_0$ the true colour index of the star. Due to the strong correlation between the colour of a star and its effective temperature, as well as the correlation between a star's absolute magnitude and its luminosity, photometric measurements allow for an observational Hertzsprung-Russell diagram to be constructed by plotting the absolute magnitude against the colour (Budding & Demircan 2007).

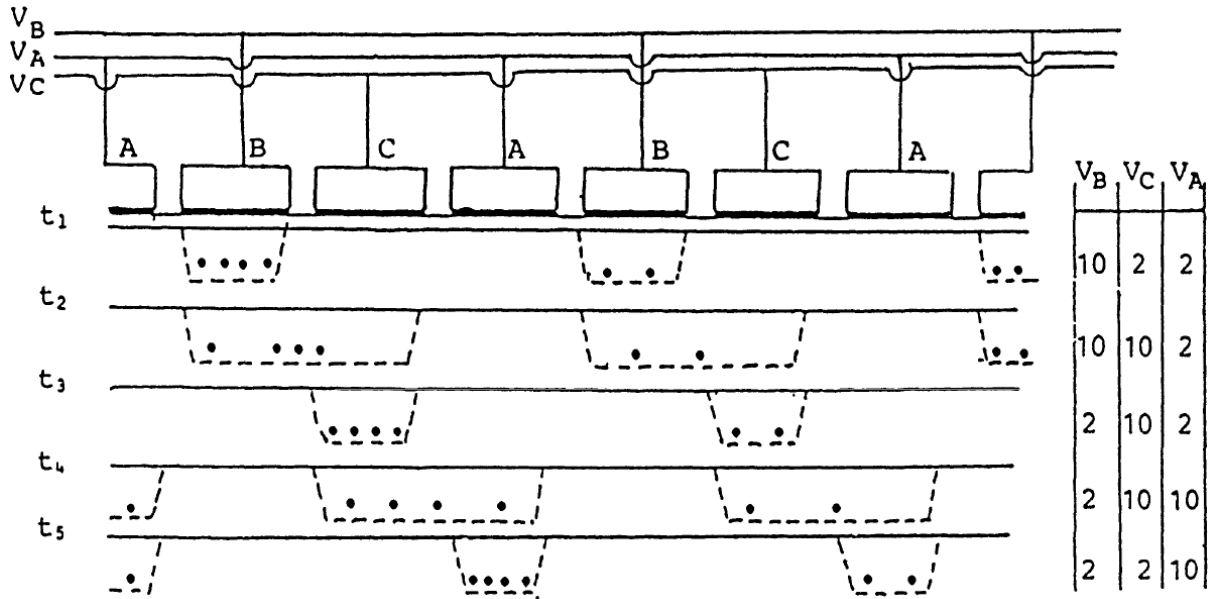


Figure 11: The charge transfer within a CCD in one row (Kovalevsky 2002).

The observations are usually carried out using charge-coupled device (CCD) detectors, since their quantum efficiency is very high (Budding & Demircan 2007). An imaging detector consists of a grid of electrodes on a semiconductor plate (e.g. p-doped silicon), with an insulating layer separating the electrodes from the plate. In the semiconductor plate, the photoelectric effect takes place, with the number of photoelectrons being proportional to the light that is received. An electrode attracts these photoelectrons, gathering them in front of the electrode, but they do not reach the electrode due to the insulating layer. These gathering areas are separated by potential walls within one row, while each row is separated from the neighbouring rows by permanent insulation walls. Overall, the image is now given as a grid of electric charges, each proportional to the number of photons arriving at the corresponding positions on the plate. Usually, three-phase CCDs are used, where three electrodes belong to each CCD pixel. The readout of the data is accomplished as depicted in Figure 11. In one row, one electrode with a high potential (B), where the photoelectrons are gathered, has two further electrodes with a lower potential next to it (A and C). This potential must be low enough so no electrons gather there. Then, the potential of C is adjusted to that of B and the charge is distributed along B and C. Next, the potential of B is set to the low potential and all the electrons gather at C. The previous steps are repeated with C and A, then with A and B and so on, so the charge belonging to a certain pixel travels along the row with minimal losses and the individual charges can be read out at the end. This is done for all rows at the same time, and a matrix containing numbers reflecting the charges, and thus intensities at each position, can be constructed (Kovalevsky 2002).

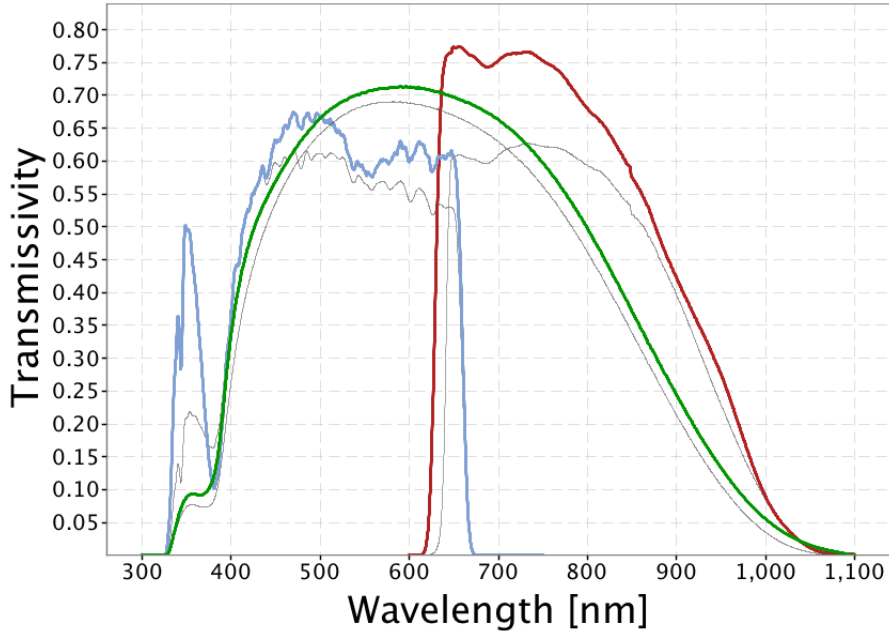


Figure 12: Gaia passbands for G (green), G_{BP} (blue) and G_{RP} (red). The grey lines are the pre-launch passbands (Evans et al. 2018); i.e. the passbands derived from models of most of the factors contributing to its definition (Jordi et al. 2010).

Gaia Photometry

In Gaia, three passbands are used: the G band (wavelength range 330 to 1050 nm), the G_{BP} band (wavelength range 330 to 680 nm, blue) and the G_{RP} band (wavelength range 640 to 1050 nm, red). While photometric measurements in the G band are performed by the same CCDs as the astrometric measurements, separate CCDs are dedicated to blue and red photometry. Gaia's photometric instrument uses the same telescopes, focal plane and Sky Mapper function for object detection as the astrometric instrument described in the previous section, recording the spectral energy distribution of objects at the same angular resolution and epoch. Two fused-silica prisms are placed before the focal plane where two strips of 7 CCDs detect the incoming light (see Figure 6). One of the two prisms, labelled BP (blue photometer), encompasses the wavelength range from 330 to 680 nm, while for the other one, labelled RP (red photometer), the range from 640 to 1050 nm is covered. The passbands, determined by coatings applied to the prisms, telescope transmission as well as detector quantum efficiency, are depicted in Figure 12.

Objects are dispersed across approximately 45 pixels in AL direction. The selected AL window size is 60 pixels so the background can be subtracted. In AC direction, the BP and RP spectra are binned over 12 pixels, yielding one-dimensional AL spectra. The maximum object density is 750 000 objects per square degree, beyond that only the brightest sources are measured (Gaia Collaboration, Prusti et al. 2016).

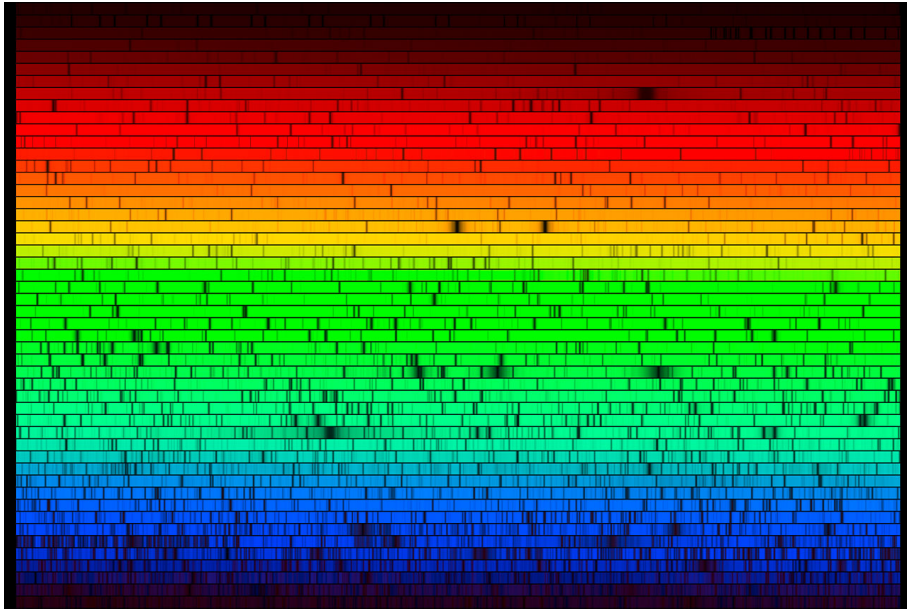


Figure 13: Échelle spectrum of the Sun¹.

2.3 Spectroscopy

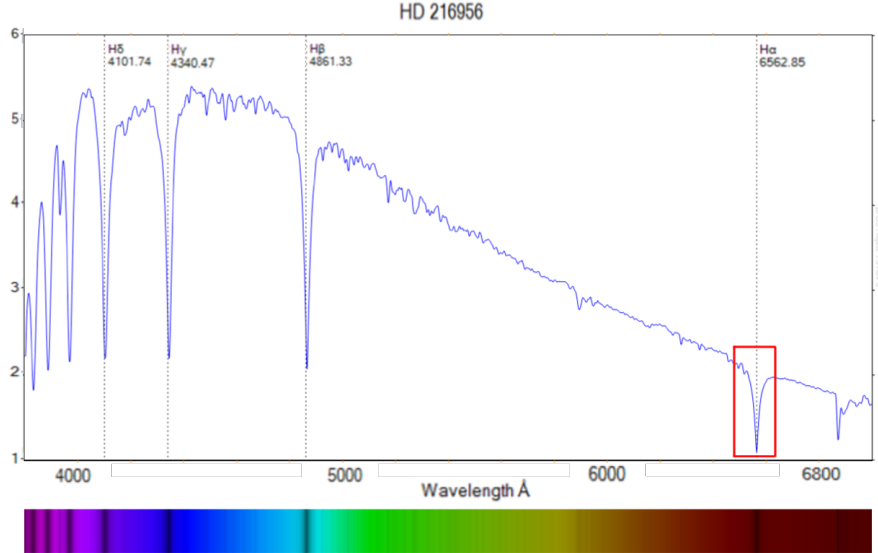
Almost all information on extrasolar objects is obtained through the analysis of electromagnetic radiation. Depending on the instruments used for the observations, the recorded information can be divided according to its resolution: low-resolution observations can be used to record the positions and magnitudes as well as broad-band colours of objects (see Section 2.1 and Section 2.2), whereas from medium-resolution and high-resolution spectra, many other astrophysical parameters can be determined, using insights from atomic and molecular physics. These include the chemical composition by considering the lines in the spectra and which atoms/ions/molecules have such transitions; the temperature and density of the environment of the system by deriving which states of an atom the transitions arise from and thus inferring the degree of excitation, which is tied to the aforementioned quantities; the abundance of a certain atom/ion/molecule by examining line strengths; motions by looking at the Doppler shift; magnetic fields by observing the splitting of lines due to the Zeeman effect, where the extent of separation is proportional to the strength of the magnetic field; and more (Tennyson 2005). Therefore, knowing the important spectral lines, energy level structure of atoms/ions/molecules as well as the intrinsic line strength and exact rest wavelength of the relevant transitions is central to the task of analysing spectra. In Figure 13, the spectrum of the Sun is portrayed in high resolution, where a great number of spectral lines are observable. The spectrum was divided up into many small parts which are depicted above each other using a so-called Échelle spectrometer.

As described above, raising the spectral resolution

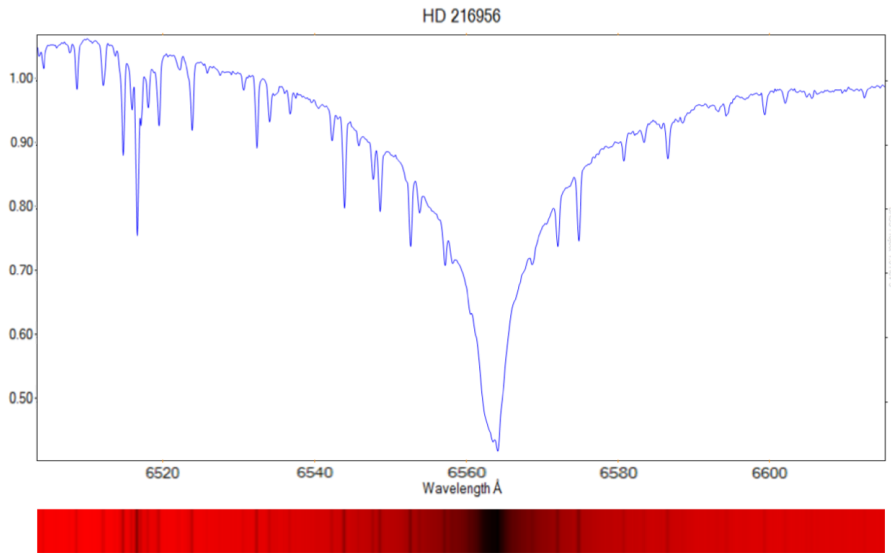
$$R = \frac{\lambda}{\Delta\lambda}, \quad (15)$$

where λ is the observed wavelength and $\Delta\lambda$ the full width at half maximum (FWHM) of unresolved spectral lines, boosts the amount of information derived from the spectra. However, recording high-resolution spectra with a good signal-to-noise ratio takes much longer than it does for low-resolution spectra and usually, high-resolution spectra are recorded one at a time, while low to medium-resolution spectra are often taken with multiobject spectrometers, so the spectral resolution at which objects are observed ought to be appropriate for the scientific task at hand to avoid inefficiency and increased cost (Appenzeller 2013). Here, *low-resolution* refers to resolutions R of up to a few hundred, *medium-resolution* to resolutions from a few hundred to a few thousand, and *high-resolution* to resolutions upward of a few thousand. In Figure 14, a low-resolution ($R = 526$ at 6532 \AA) and a high-resolution ($R = 7254$ at 6532 \AA) spectrum of Fomalhaut (HD216956) are shown. Figure 14b shows only a small range around the $\text{H}\alpha$ line. As can be seen, many more lines not visible in the low-resolution spectrum emerge, enabling a more in-depth analysis.

¹<https://www.eso.org/public/images/sunspectrum-noao/>, retrieved 05.08.2020



(a) Low-resolution spectrum: $R = 526$ at 6532 Å .



(b) High-resolution spectrum: $R = 7254$ at 6532 Å .

Figure 14: Spectra of Fomalhaut (HD 216956)², which has the spectral type A3V, an effective temperature $T_{\text{eff}} = 8751 \text{ K}$ and a surface gravity $\log g = 4.21$ (Di Folce et al. 2004). The red rectangle marks the range shown in the high-resolution spectrum.

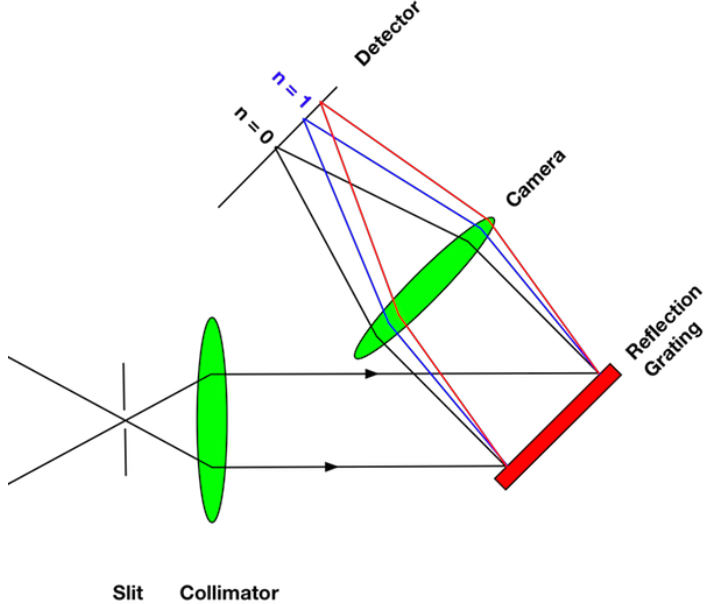


Figure 15: Optical layout of basic slit spectrometer³.

Generally, most astronomical spectrometers are based on the layout shown in Figure 15. A slit is located in the focal plane of the telescope, and a target should be positioned such that their light enters the slit vertically. The slit is followed by a collimator making the beams parallel. These beams hit a disperser (which is a reflection grating in Figure 15, but could also be a prism, grism etc.), which reflects the beams in different angles for different wavelengths. Finally, another mirror (labelled Camera in Figure 15) focuses the beams onto the detector, merging beams of the same wavelength back together. However, in the 0th order, no separation takes place (Appenzeller 2013).

Reflection grating is shown schematically in Figure 16. If the incident angle (which is the angle between the incoming beam and the normal to the grating plane) is Θ_i , the diffracted angle (which is the angle between the diffracted beam and the normal to the grating plane) is Θ_m , the grating period is d , and the wavelength of the incoming beam is λ , the condition for constructive interference is

$$n\lambda = d(\sin(\Theta_i) - \sin(\Theta_m)), \quad (16)$$

as is shown in Figure 16. $n = 0, 1, 2, \dots$ refers to the diffraction order. From this,

$$\Theta_m = \arcsin \left(\sin(\Theta_i) - \frac{n\lambda}{d} \right) \quad (17)$$

can be derived, which demonstrates the wavelength dependence of the diffraction angle.

As an example of a grating spectrograph, the ESO Multi-Mode Instrument (EMMI) at the New Technology Telescope (NTT) on the La Silla Observatory is briefly discussed. A schematic layout is given in Figure 17, which is taken from the EMMI User's manual⁴, as is the following information.

The blue “arm” is used in the wavelength range 300 nm to 500 nm, while the red “arm” is intended for wavelengths between 400 nm and 1000 nm, with two possible paths that the light can take in each arm, giving four modes of observation in total: RILD (Red Imaging and Low-Dispersion spectroscopy), REMD (REd Medium Dispersion spectroscopy), BIMG (Blue IMaGing) and BLMD (BLue Medium Dispersion spectroscopy). The light

²<http://jazzistentialism.com/blog/?p=1661>, retrieved 04.08.2020

³<http://slittlefair.staff.shef.ac.uk/teaching/phy217/lectures/instruments/L16/index.html>, retrieved 04.08.2020

⁴<http://www.ls.eso.org/sci/facilities/lasilla/instruments/emmi/emmiManual.html>, retrieved 04.08.2020

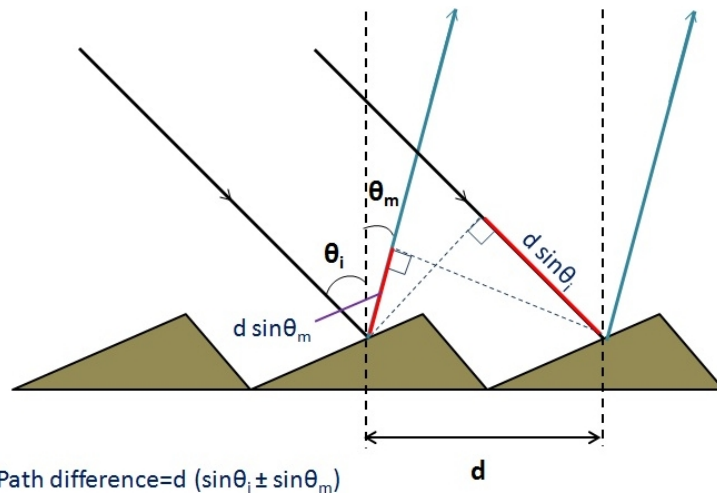


Figure 16: Reflection grating and grating equation (Source: Wikipedia).

paths for the imaging modes lead straight towards the cameras, while the light paths for grating spectroscopy are guided through the prism wheel and grating units first; all paths are indicated by dashed lines in Figure 17. Some important components include: four filter wheels, namely a blue and a red imaging wheel as well as a blue and a red below-slit wheel, where the red imaging wheel is tilted by a 5° angle to circumvent reflections between the CCD and the filter; a grism wheel, but just in the red arm; one grating unit in each arm, employed in medium-resolution spectroscopy; a slit unit in the red arm where so-called starplates can be inserted, referred to as the starplate wheel, which contains slit(s) for the object(s) observed; and a medium-dispersion slit for grating spectroscopy (MD slit). In each arm, a CCD camera is used as a detector.

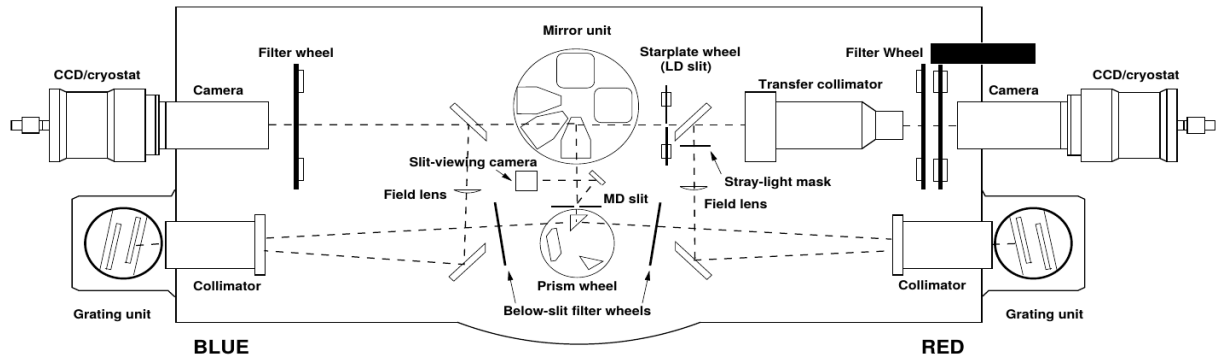


Figure 17: Layout of EMMI.

Low-resolution spectroscopy is done in RILD mode. One of the grisms available in the grism wheel is combined with a fixed slit (starplate), the width of which can be $0.5''$, $1.0''$, $1.5''$, $2.0''$, $5.0''$ or $10''$, with a length of $8'$ in each case. If necessary, an order-sorting filter is included. The choice of the grism determines the wavelength range, as the grisms cannot be rotated. Multi-object spectroscopy is carried out similarly, but custom starplates with several slitlets are put in place of the fixed slits mentioned above.

For medium-dispersion spectroscopy, the REMD or BLMD mode is used. The respective grating is combined with the MD slit and an order-sorting filter if necessary. The width of the slit can be chosen between $0.4''$ and $8.5''$, while the length is $330''$. However, the length can be limited by a decker, down to $3''$. The rotation of the gratings, which can be adapted accordingly, determines the wavelength range. There are four different gratings in the red arm and five in the blue arm with varying grating periods, blaze angles, dispersions etc., two of which are available at a time for each arm. Échelle spectroscopy, which can be carried out in the REMD mode, will not be discussed.

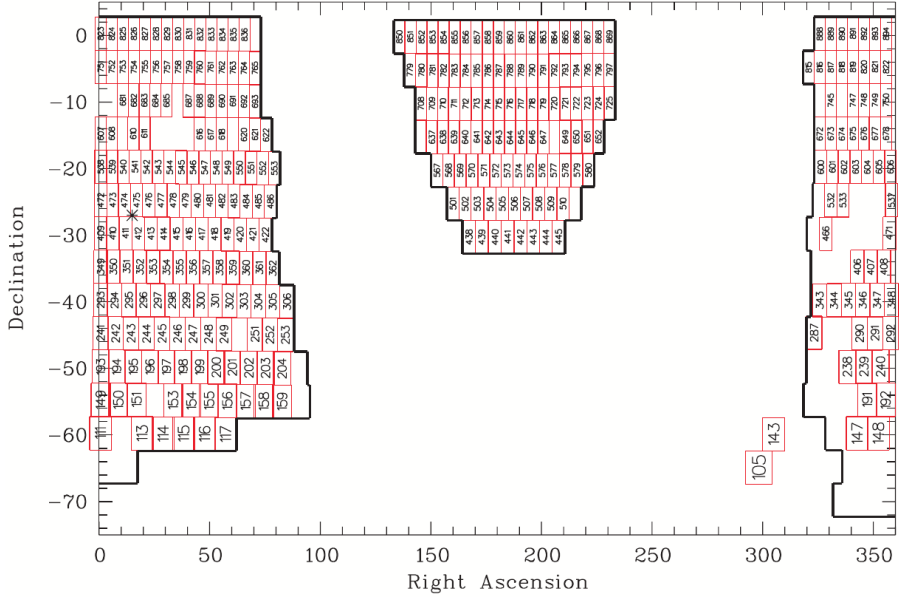


Figure 18: The survey area. Individual fields and their numbers are given in the small red rectangles (Christlieb et al. 2001).

3 The Sample

3.1 The Hamburg/ESO Survey

The Hamburg/ESO Survey (HES) is an objective-prism survey, originally designed for the study of quasi-stellar objects (QSOs). The aims, as outlined by Reimers & Wisotzki (1997), were the compilation of a list of QSOs to be observed in detail by ESO's Very Large Telescope (VLT), the search for gravitational lenses, finding bright QSOs unaffected by absorption and expanding the catalogue of QSOs on the bright end. However, due to the spectral resolution, which is better than 15 \AA at $H\gamma$, the stellar content of the HES can be explored as well, e.g. metal-poor halo stars, white dwarfs, hot subdwarfs and carbon stars (Christlieb et al. 2001).

The observations were carried out using ESO's 1-metre Schmidt telescope with an objective prism having a prism angle of 4° . This results in a relatively high dispersion of 450 \AA/mm at $H\gamma$ (Reimers & Wisotzki 1997). The spectral plates used were Kodak IIIa-J of size $28 \times 28 \text{ cm}^2$, corresponding to a solid angle of 25 deg^2 at an imaging scale of $67.5''/\text{mm}$ (Wisotzki et al. 1996). The spectral range of these plates is approximately 3200 \AA to 5300 \AA . On the blue end, it is given by the atmospheric cutoff, while the cutoff on the red end is a result of the sensitivity function of the IIIa-J plates. The scanning of the plates was performed by a PDS microdensitometer, dividing the plates up into four sections of 7500×7500 pixels each (Christlieb et al. 2008).

The survey area comprises 380 fields, for each of which a plate was taken. Roughly speaking, this area is characterised by the three conditions $+2.5^\circ > \delta > -78^\circ$, $\Sigma < 100$ stars per square degree and $N_{\text{H}} < 10^{21}/\text{cm}^2$, where δ is the declination, Σ the density of stars and N_{H} the column density of hydrogen (Christlieb 2000). The HES area is illustrated in Figure 18. Due to overlapping spectra as well as plates, the actual area is reduced from 8853 deg^2 to 6726 deg^2 . The spectral resolution is about 10 \AA at the CaII K line ($\lambda = 3934 \text{ \AA}$) and primarily seeing-limited (Christlieb et al. 2008); under good seeing conditions, the spectrum is under-sampled, so the resolution is sampling-limited (Christlieb 2000).

The HES uses direct plates from the Digitized Sky Survey I (DSS-I) as its input catalogue: an astrometric transformation between the DSS-I direct images and the recorded plates is computed (after the background is determined and subtracted). This can be done down to a magnitude limit of $B_J \simeq 21$, however, the formal limit is set at two times the rms background noise of the spectral image, giving a limit of ~ 18 to 18.5 mag. The bright end is determined by the saturation of the photographic spectra but can go as high as $B_J \simeq 11$ if partly saturated spectra are included (Wisotzki et al. 2000). On the direct plate, objects in the dispersion direction are searched for to identify

overlapping spectra, since these would disturb later analyses. The digitisation and reduction process also includes the classification of the sources: `stars` refers to point-like sources, `ext` refers to sources that are extended on the plates, and `bright` refers to sources where the spectra on the plates are almost in saturation. Depending on the type, the extraction process differs, but in each case, the process maximises the signal-to-noise ratio. After the wavelength calibration (determining the wavelength zeropoints), the spectra are stored as MIDAS frames, each with a MIDAS table that includes other properties of the corresponding stars, such as its position, brightness and more (Christlieb 2000).

Several example spectra are shown in Figure 19, with the range around the CaII H and K lines displayed in greater detail. In the upper spectrum, no CaII K line is seen; in the second one, it is unclear whether the CaII K line is present; in the third one, a weak CaII K line is detected; and in the last spectrum, the CaII K line is strong.

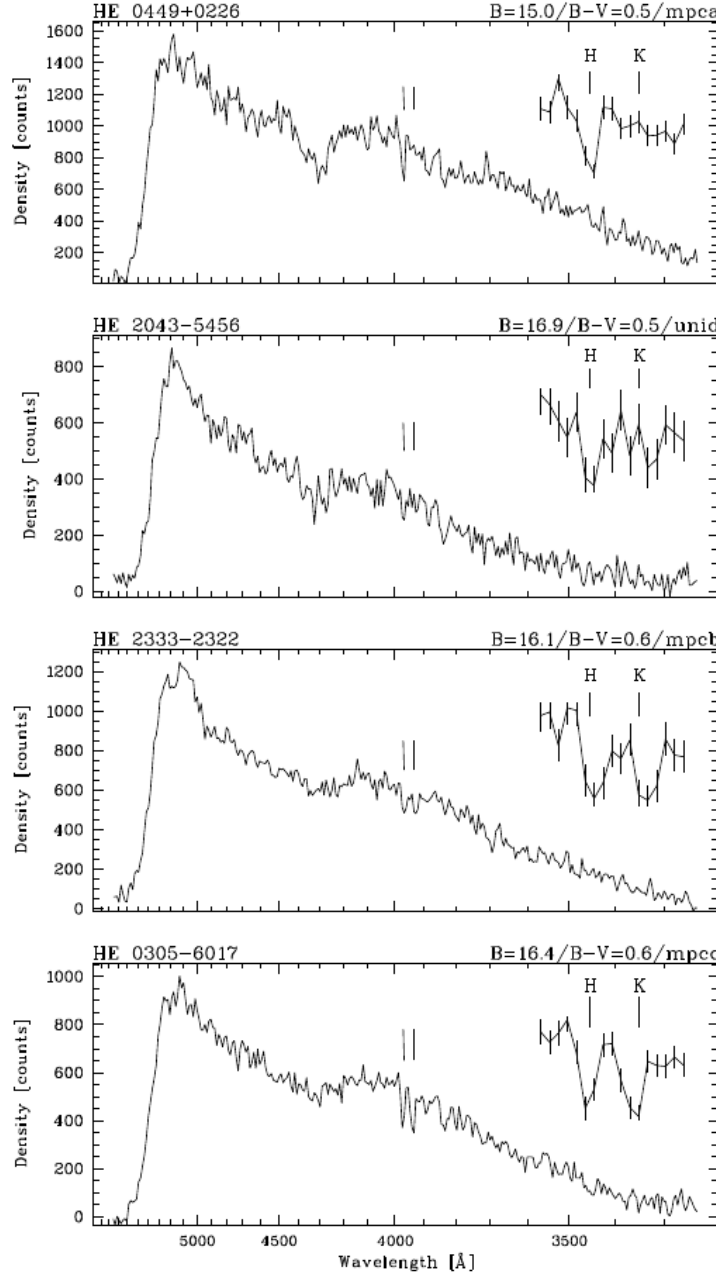


Figure 19: Examples of spectra taken in the HES (Christlieb et al. 2008).

For the photometric data, the direct plates are calibrated with individual photometric sequences; the spectral plates

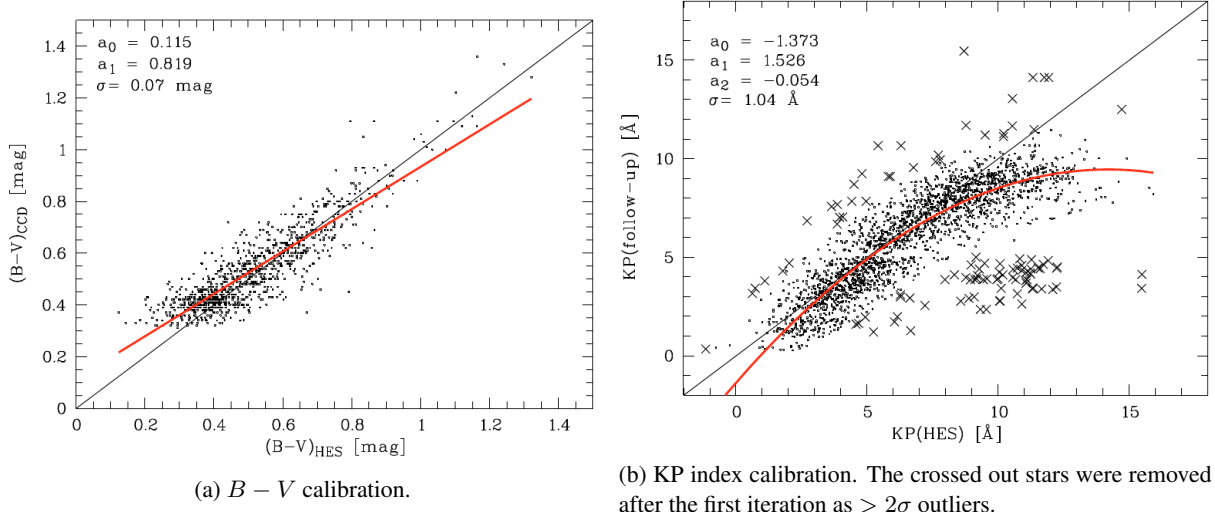


Figure 20: Calibrations (Christlieb et al. 2008).

are then calibrated with these magnitudes, yielding an accuracy better than 0.2 mag for B_J . The B_J magnitude is characterised by the sensitivity function of the Kodak IIIa-J and the filter curve of a Schott GG395 filter. For main-sequence stars with colours $-0.1 < (B - V) < 1.6$, it is related to B via

$$B = B_J + 0.28(B - V). \quad (18)$$

The $B - V$ colour can be approximately determined from the HES spectra with an accuracy of about 0.1 mag (Christlieb et al. 2008). The average pixel-wise signal-to-noise ratio depends on the B_J magnitude, although the scatter is quite large due to varying plate background and seeing (Christlieb 2000).

The HES data base contains 12 357 153 digital spectra from 379 plates. Due to the quality of the spectra, allowing for the CaII K line to still be detected even in quite metal-poor stars, the HES is well-suited for a search of metal-poor stars: since there is a trend for almost all stars in the Galaxy regarding [Ca/Fe], the CaII K line serves as an indicator for [Fe/H] and the HES spectra can be systematically analysed (Christlieb et al. 2008).

3.2 Sample selection

In this subsection, the selection procedure for the sample of candidate metal-poor stars used in this thesis is described. It is based on cutoff lines in line index-colour diagrams determined from randomly generated values. The following paragraphs all refer to the article on the construction of the sample by Christlieb et al. (2008), where a more detailed description can be found.

The calibration of the $B - V$ colours of objects, which were first determined directly from the spectra as described in Christlieb et al. (2001), was done using 1039 metal-poor stars from the HK survey with accurate CCD photometry that were also recorded by the HES. Objects with overlapping HES spectra were disregarded and a linear fit was carried out, the result of which is shown in Figure 20a. Notably, the 1σ uncertainty is as small as 0.07 mag.

Line indices are used to quantify the extent of the integrated absorption of lines by relating the depth of a line to the continuum level. The KP index, belonging to the CaII K line, and the GP index, belonging to the CH G band, were determined according to Beers et al. (1999). The calibration of the KP index was carried out using more than 2000 HK survey stars for which medium-resolution ($\Delta\lambda \sim 2$ \AA) spectra were available. The KP indices from these stars were compared to those measured in the HES spectra for the same stars. Since the resolution of the HES spectra is not sufficient to distinguish between 6 \AA, 12 \AA and 18 \AA bands, a single 26 \AA wide band, which is centred on the CaII K line, was utilised. The result of the calibration is shown in Figure 20b. The calibration of the GP index was done similarly.

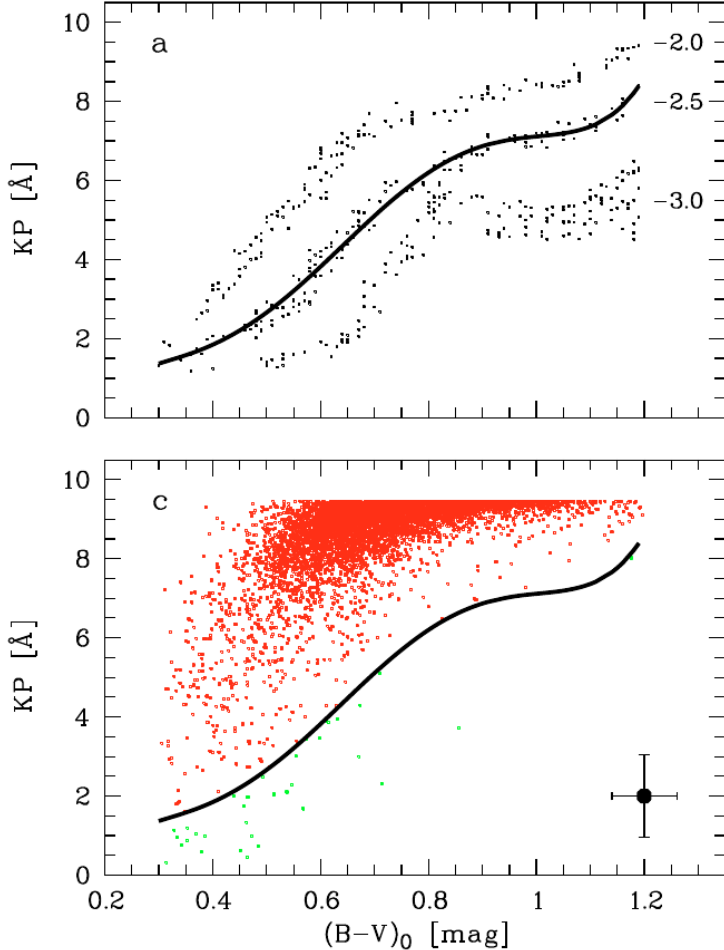


Figure 21: Upper image: Determination of the cutoff line. For $(B - V)_0 < 0.45$ and $(B - V)_0 > 1.00$, the weight of the data points was multiplied by ten. Lower image: Application to all objects in ESO field 147 (Christlieb et al. 2008).

In total, three selection criteria were devised. The first uses a cutoff line in a KP- $(B - V)_0$ -diagram. To determine this cutoff line, 10 000 stars were simulated with values of $0.3 < (B - V)_0 < 1.2$ and $0.0 < \text{KP} < 12.0$ randomly distributed. For each star, $[\text{Fe}/\text{H}]$ was then calculated from $(B - V)_0$ and KP, based on the method from Beers et al. (1999). A fifth order polynomial fit was carried out using the data points in the range $[\text{Fe}/\text{H}] = -2.4$ to $[\text{Fe}/\text{H}] = -2.6$ (see Figure 21). If an object is below the cutoff line and fulfills some additional conditions such as a signal-to-noise ratio of at least 5, the line being significantly detected at all and the spectrum not being an overlapping spectrum, it is considered a metal-poor candidate. The reddening which was applied to $B - V$ to obtain $(B - V)_0$ was taken from the maps of Schlegel et al. (1998).

The second criterion is similar, but uses $(J - K)_0$ instead of $(B - V)_0$, J and K being magnitudes used by 2MASS. They were obtained by crossmatching the HES and 2MASS. The cutoff line was determined using a fourth order polynomial and is limited to the range $0.2 < (J - K)_0 < 0.75$. The third criterion is to simply include objects as candidates if the CaII K line is not sufficiently observed in the HES spectrum, since near the main-sequence turnoff, the object could be erroneously rejected based on its KP index due to noise leading to a greater KP index.

HES objects classified as `stars` were selected, if any of the three conditions is fulfilled, while for objects classified as `bright`, either the second or third condition was sufficient for selection. Those of type `ext` were excluded so that no galaxies were accidentally selected. In a second step, all candidates were checked visually and objects that showed clear plate artifacts, overlapping spectra, or were clearly identified as galaxies, cool white dwarfs etc. were removed. A comparison to 1121 HK survey stars demonstrated that most stars with $[\text{Fe}/\text{H}] > -2.0$ should be rejected by the selection criteria, while on the low-metallicity end, the sample should be almost complete.

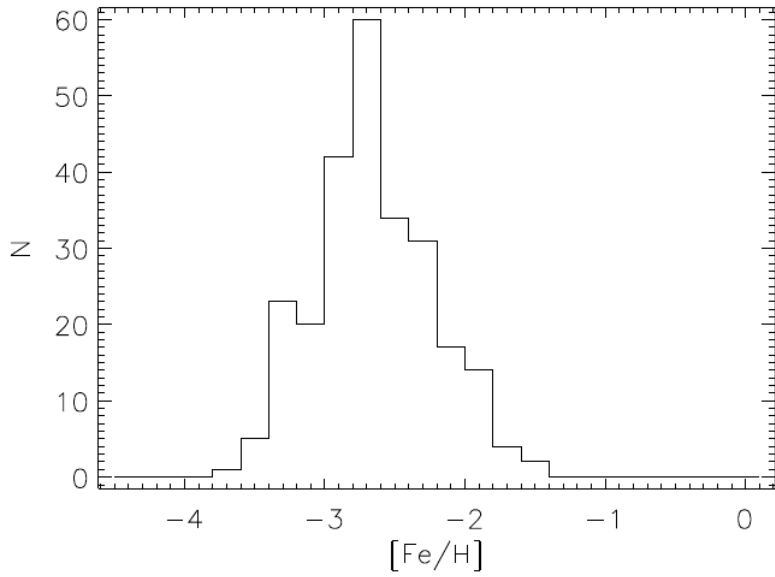


Figure 22: Distribution of metallicities from final spectral analysis (Barklem et al. 2005).

After applying the selection criteria to all 379 HES fields, the visual inspection, and removal of stars which appeared on multiple plates, the final sample consists of 20 271 stars, as published by Christlieb et al. (2008). In their Appendix A, a list of the parameters published for each star can be found.

Beers et al. (2007) compiled a sample of 1857 stars and determined their broadband $UBVR_{\text{C}}I_{\text{C}}$ photometry. This sample will also be used in the analysis. The stars are taken from the thick-disc and halo population of the Galaxy, and 1221 stars were selected as candidate metal-poor stars as well as 576 as candidate field horizontal-branch or other A-type stars (FHB/A), all of which were taken from the HK and Hamburg/ESO surveys. A smaller number were selected from other surveys, either as candidate metal-poor, candidate FHB/A or candidate RR Lyrae stars. For all of the stars in the sample, medium-resolution spectroscopy is available. The parameters given in the sample include the V magnitude and several colour indices (e.g. $B - V$, $U - B$, etc.) as well as the reddening $E(B - V)$, once again determined from the Schlegel et al. (1998) maps.

A third sample of 253 stars used in this thesis comes from the Hamburg/ESO R-process Enhanced Survey (HERES), which took "snapshot" spectra of 373 confirmed metal-poor stars mostly stemming from the HES. In Barklem et al. (2005), 253 of these, chosen such that they do not contain strong molecular carbon features, were spectroscopically analysed. In particular, the effective temperature, surface gravity and metallicity were determined. The effective temperature was estimated from the colour calibrations of Alonso et al. (1999) by taking the average of the estimates obtained from different colours. The rms error was estimated at 100 K, considering the photometric errors, the error in the reddening and the fact that not all colours were available. The metallicities and surface gravities were determined in the automated spectrum analysis described in Barklem et al. (2005) after initial estimates. The metallicity distribution of the sample is shown in Figure 22.

4 Data analysis

4.1 Crossmatch

Since the observations carried out by the Gaia satellite include more precise astrometry and photometry as well as the possibility to derive important additional parameters (such as the distance from the parallax), the analysis makes use of Gaia data. This means that the first task is to identify the sources in the samples with the corresponding Gaia DR2 sources. The identification algorithm initially included the following steps:

1. Within a search radius of 3 arcseconds around the HES source, find all Gaia sources. The radius of 3 arcseconds is motivated by the 1σ uncertainty in position of the HES sources being on the order of 1 arcsecond.
2. A plausibility check by converting the Gaia photometric data into the B magnitude and $B - V$ colour and comparing them to the values given in the HES sample. Since the 1σ uncertainties of the B magnitude and $B - V$ colour are ~ 0.2 mag and ~ 0.1 mag (Christlieb et al. 2008), respectively, the identification between a HES source and a Gaia source is considered plausible, if the B magnitude calculated from Gaia data is within 0.6 mag of the HES B magnitude and the $B - V$ colour is within 0.3 mag of the HES $B - V$ colour; in other words, if the magnitude and colour fall within the 3σ range.
3. Using the proper motions of the Gaia sources within the search radius around each HES source and the time difference between the epoch of the DSS-I plate of the corresponding field and of the Gaia DR2 coordinates, the position of the Gaia sources at the time the DSS-I plates were taken can be determined. The equinox is J2000.0 for all three HES samples used, while Gaia uses the ICRS as its reference system. The offset of 78 mas between the ICRS and J2000.0 (Folkner et al. 1994) is neglected.
4. The Gaia source identified with the HES source is the one now closest to it.

Starting with the sample of 20271 stars from Christlieb et al. (2008), the first step is done using the CDS X-Match Service⁵, which outputs a file containing all matches within a radius of 3 arcseconds of each HES source. There are 19576 HES sources to which only one Gaia source is assigned, 443 HES sources to which two Gaia sources are assigned, and only one HES source with three Gaia sources within a 3" radius.

To conduct the plausibility check, photometric relationships taken from Evans et al. (2018) are used to determine $(B - V)_{\text{Gaia}}$ and B_{Gaia} from Gaia's photometric data to compare to $(B - V)_{\text{HES}}$ and B_{HES} . In their Table A.2, the two polynomials

$$G - V = -0.01760 - 0.006860 \cdot (BP - RP) - 0.1732 \cdot (BP - RP)^2 \quad \text{and} \quad (19)$$

$$G - V = -0.02907 - 0.02385 \cdot (B - V) - 0.2297 \cdot (B - V)^2 - 0.001768 \cdot (B - V)^3 \quad (20)$$

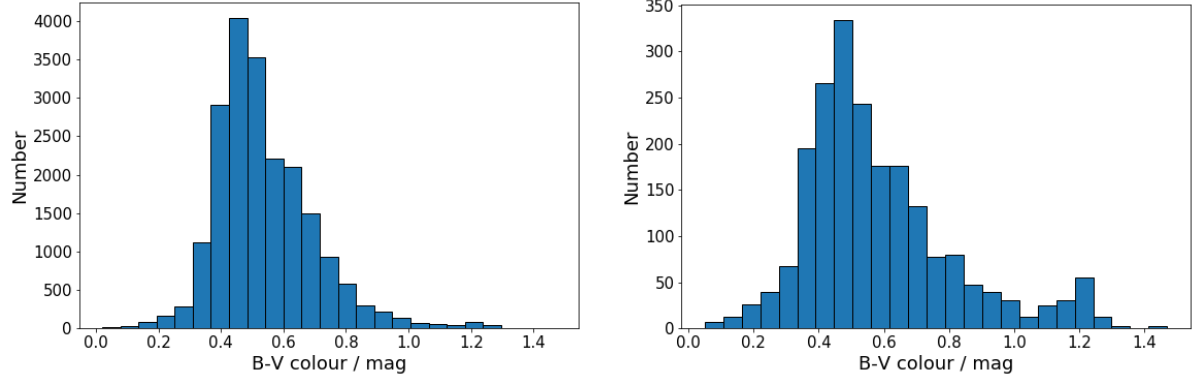
can be found. Since no direct transformation between $BP - RP$ and $B - V$ is given, $(B - V)_{\text{Gaia}}$ is derived by equating (20) and (19). Solving for $B - V$ yields three solutions, of which the physically reasonable one can be chosen. As per equation (19), the V_{Gaia} magnitude is given by

$$V = G + 0.0176 + 0.006860 \cdot (BP - RP) + 0.1732 \cdot (BP - RP)^2, \quad (21)$$

so the B_{Gaia} magnitude is then determined using $B_{\text{Gaia}} = (B - V)_{\text{Gaia}} + V_{\text{Gaia}}$. The plausibility check is carried out comparing $(B - V)_{\text{Gaia}}$ and B_{Gaia} to $(B - V)_{\text{HES}}$ and B_{HES} of the corresponding HES source. All Gaia sources failing the criterion mentioned above are discarded. Figure 23 depicts the statistical distribution of colours of removed stars. As shown, stars on the red end are discarded more often in comparison to other stars. This is probably due to uncertainties in the calibration of $B - V$ as described in Christlieb et al. (2001): only few stars were available for the fit beyond $B - V > 1.0$, which means that the calibration is not very reliable in that range.

As it turns out, the plausibility check already removed any multiple assignments within the 3" radius, and the objects left after the plausibility check now all have only one Gaia source assigned to them. This means that step three and four of the algorithm are dropped and the identification process is finished. The number of HES sources to which a Gaia source could be assigned is 18373 out of 20271 stars.

⁵<http://cdsxmatch.u-strasbg.fr/>, retrieved 30.07.2020



(a) Histogram of $B - V$ colours of all HES sources from Christlieb et al. (2008). (b) Histogram of $B - V$ colours of HES sources that were discarded based on the plausibility check.

Figure 23: Statistical distribution of colours.

In order to verify the $3''$ search radius, initially chosen as it corresponds approximately to a 3σ radius around the object, a histogram of the angular distances between the HES sources and the corresponding Gaia sources is plotted (Figure 24). The maximum of the distribution is around $0.7''$ as opposed to close to zero, which could be explained by a systematic error in the astrometry of the direct plates used for the HES, which would result in a Gaussian distribution as seen in the figure. The objects in the tail of the distribution towards the limit of $3''$ include comparatively more objects with significant proper motion, as shown in Figure 25. A second way of verifying the

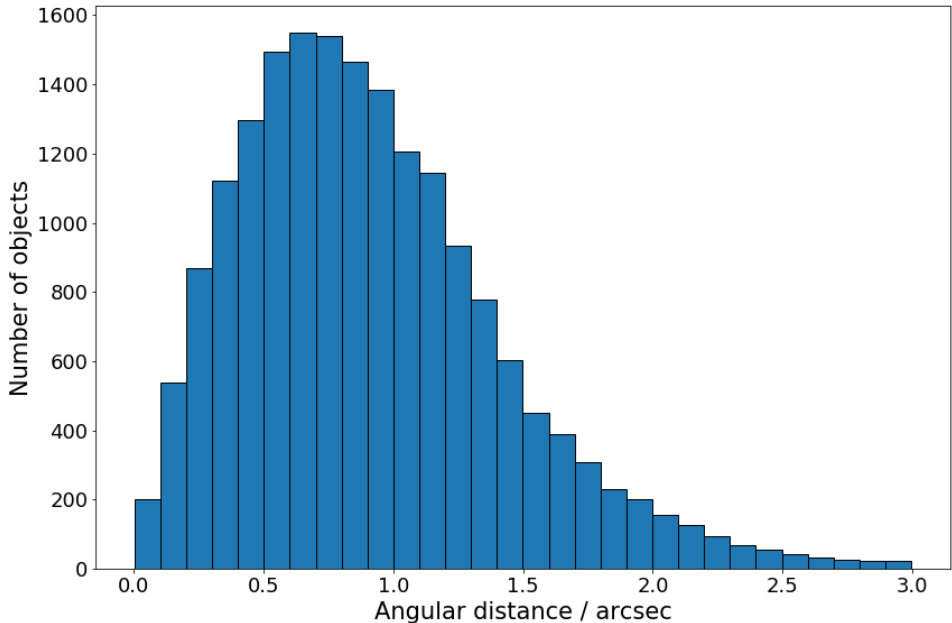
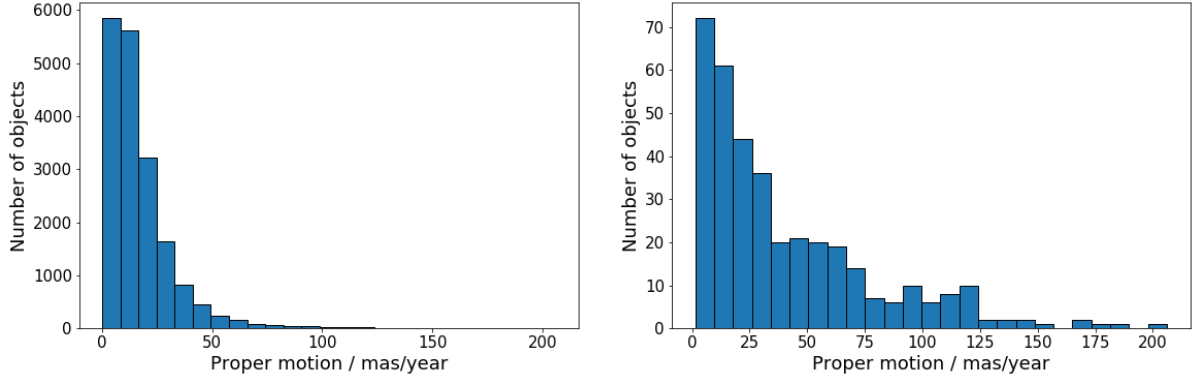


Figure 24: Histogram of the angular distance between object and matched object.

search radius makes use of the epoch differences and proper motions mentioned before. From Gaia DR2 data, the absolute value of the proper motion of each object is determined using

$$\mu = \sqrt{\mu_\alpha^2 + \mu_\delta^2 \cos^2(\delta)}, \quad (22)$$

where μ_α is the proper motion in right ascension direction, μ_δ is the proper motion in declination direction and the factor $\cos(\delta)$ takes into account the declination δ of the object. Retrieving the epochs at which DSS-I plates of each field were taken as well as the Gaia epochs, and checking which field each object is located in allows for the



(a) Histogram of proper motions of all sources in the HES sample. (b) Histogram of proper motions of sources where the angular distance between object and matched object is larger than $2.2''$.

Figure 25: Distribution of proper motions.

determination of the epoch difference

$$\Delta t = \text{epoch}_{\text{Gaia}} - \text{epoch}_{\text{DSS-I}} \quad (23)$$

A histogram portraying the shift of the objects is produced by plotting the distribution of $\mu \cdot \Delta t$ (Figure 26). The steep slope and the fact that only a tiny fraction of all objects lie beyond $3''$ solidify the choice of the search radius, as did Figure 24.

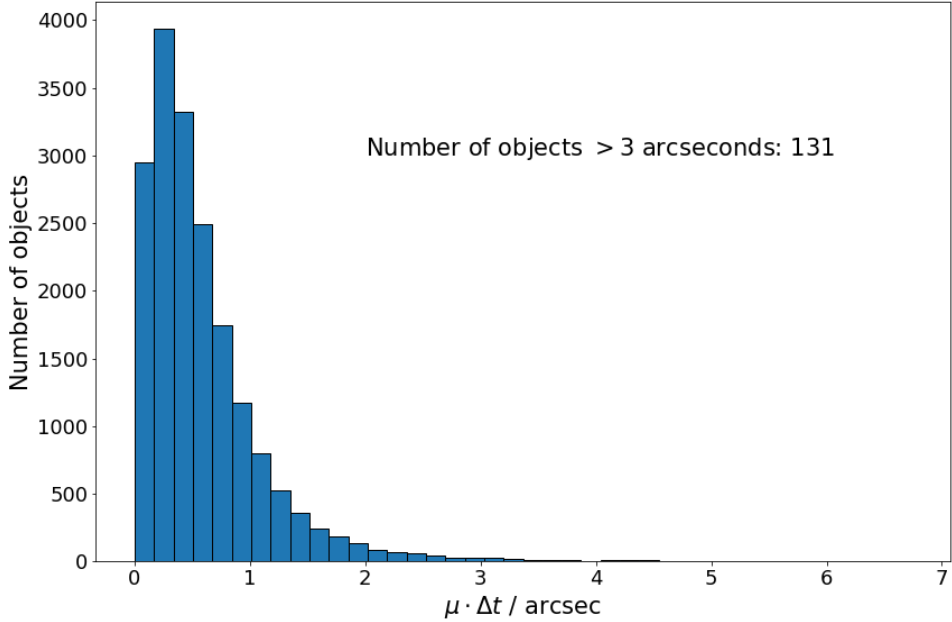


Figure 26: Histogram of the proper motion multiplied by the epoch difference between DSS-I plates and Gaia DR2.

Next, the same procedure is carried out for the sample of 1857 stars from Beers et al. (2007). Here, for 1436 HES sources, one Gaia source is found within a search radius of $3''$ and for 34 HES sources, two Gaia sources are within that radius. After performing the plausibility check, 1351 objects are left, again now each with only one Gaia object within a radius of $3''$. Instead of using the B magnitude however, the V magnitude was used (equation (21)), since no B magnitude was given in the sample. The distribution of angular distances between object and matched object is similar to Figure 24, as expected. For the sample of 253 stars from Barklem et al. (2005), 249 are identified with Gaia DR2 sources.

4.2 Colour-magnitude diagrams

As discussed in Section 2.2, knowledge of the colour and absolute magnitude of stars allows for the construction of observational Hertzsprung-Russell diagrams, also called *colour-magnitude diagrams* (CMDs). Due to the intricate connection between colour and effective temperature as well as the connection between absolute magnitude and surface gravity, and stellar parameters such as effective temperature and surface gravity (and thus, the position on the CMD) indicating the evolutionary status of a star, CMDs are important tools for the selection of candidates to take a closer look at spectroscopically. To give an example, during the red-giant branch dredge-up period, products of the CNO-cycle are mixed into the stellar atmosphere, lowering the C abundance. This means the spectrum, which reflects the composition of the stellar atmosphere, no longer exhibits the initial chemical composition after leaving the main sequence.

Before proceeding, the transformation between $B - V$ and $BP - RP$ is determined from the 18373 stars left after the crossmatch, which is necessary because it turns out that the Gaia DR2 data for the reddening $E(BP - RP)$ is absolutely unrealistic and thus unusable. According to Andrae et al. (2018), parameters, including the reddening $E(BP - RP)$, were inferred under the assumption of approximately solar metallicity and are probably wrong for low metallicity stars, which could explain the issues with $E(BP - RP)$, since the sample consists of candidate metal-poor stars.

In order to obtain the transformation, a linear and a quadratic function expressing $BP - RP$ as a function of $B - V$,

$$BP - RP = a_1 \cdot (B - V) + b_1 \quad \text{and} \quad (24)$$

$$BP - RP = a_2 \cdot (B - V)^2 + b_2 \cdot (B - V) + c_2, \quad (25)$$

are fitted to the data using least squares (Figure 27). As can be seen, throughout most of the range of values,

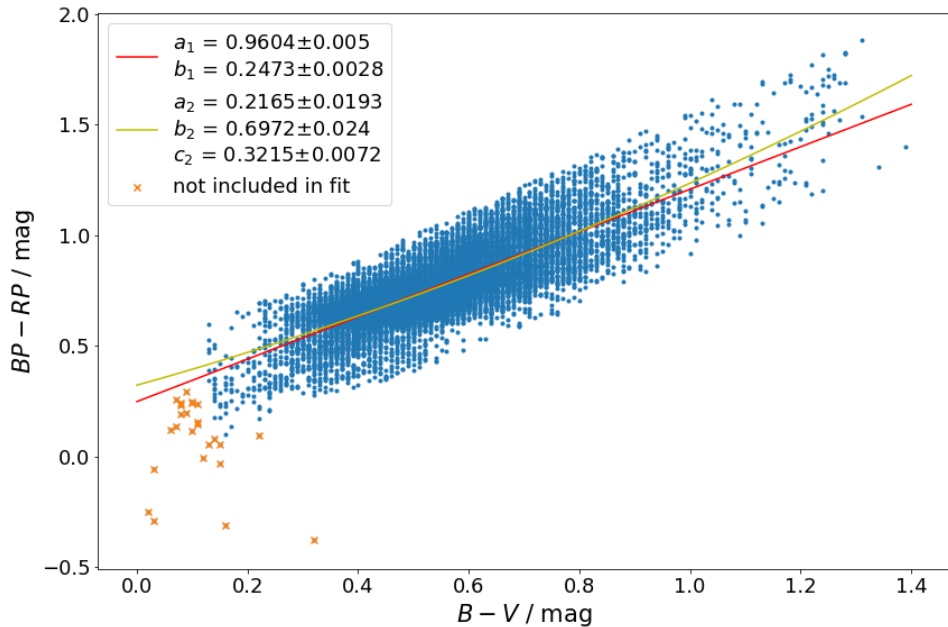


Figure 27: Transformation curves between $BP - RP$ and $B - V$. The crossed out objects are not included in the fit.

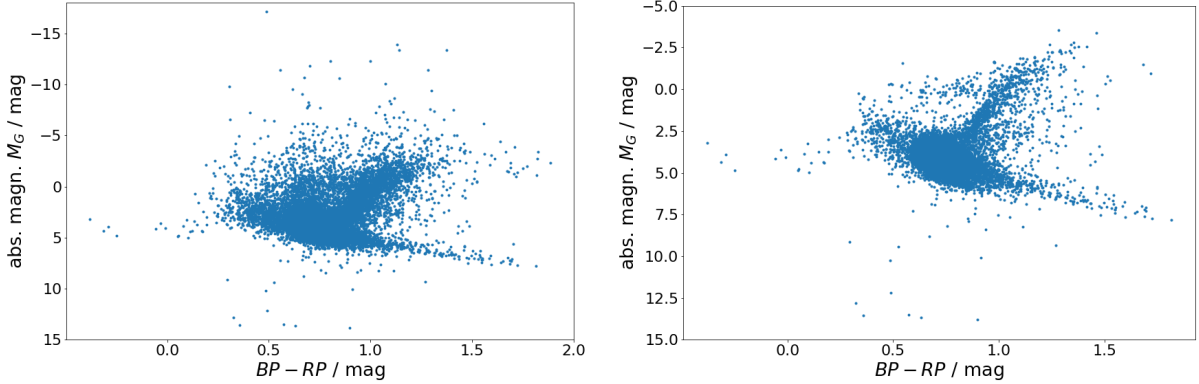
the curves are almost identical and towards the edges, where the deviation increases, much fewer data points are available, which means the fit is not very well determined there anyway. Because of this, the transformation chosen for the remainder of this thesis is the linear fit (24),

$$BP - RP = 0.2473 + 0.9604 \cdot (B - V). \quad (26)$$

To obtain the absolute magnitude M_G , equation (10) is used. While the apparent magnitude G is given in DR2, to derive the extinction in the G band A_G , the formula and coefficients from Gaia Collaboration, Babusiaux et al.

c_1	c_2	c_3	c_4	c_5	c_6	c_7
0.9761	-0.1704	0.0086	0.0011	-0.0438	0.0013	0.0099

Table 1: Coefficients for extinction A_G , taken from Gaia Collaboration, Babusiaux et al. (2018).



(a) “Naive” CMD of all ~ 18000 objects, without conditions on the parallax uncertainty. (b) CMD of objects which fulfill the condition $\sigma_\omega/\omega < 0.2$ on the parallax uncertainty.

Figure 28: CMDs before dereddening; comparison between no restriction and restriction on parallax uncertainty.

(2018) are applied. The extinction is given by

$$A_G = k_G A_0, \quad (27)$$

$$k_G = c_1 + c_2(BP - RP)_0 + c_3(BP - RP)_0^2 + c_4(BP - RP)_0^3 + c_5 A_0 + c_6 A_0^2 + c_7(BP - RP)_0 A_0, \quad (28)$$

where $A_0 = 3.1E(B - V)$, with the $E(B - V)$ values taken from the Schlegel et al. (1998) maps, as mentioned before. With the transformation (26) and the dereddened Johnson-Cousins colour $(B - V)_0$ given in the sample, the dereddened Gaia colour $(BP - RP)_0$ is determined by inserting $(B - V)_0$ into (26). The coefficients c_i are listed in Table 1.

The estimation of the distance d in equation (10) employs the parallax measurements carried out by Gaia. In general, due to geometry and the definition of a parsec, if ϖ is the measured parallax in arcseconds, the distance $d = 1/\varpi$ in parsec is a very good approximation. However, each parallax measurement is associated with an uncertainty, $\varpi \pm \sigma_\varpi$, and taking $1/\varpi \pm \sigma_\varpi/\varpi^2$ as the distance estimate turns into an inadequate approximation as the relative uncertainty grows, as demonstrated by Bailer-Jones (2015). For this reason, the condition of a relative precision of 20% is placed upon the data (see Luri et al. 2018), and only objects fulfilling $\sigma_\varpi/\varpi < 0.2$ are included in the diagrams. Negative parallaxes are also removed, finally leaving only 10205 objects. The formula for M_G thus becomes

$$M_G = G + 5 + 5 \log(\varpi/1000) - A_G \quad (29)$$

where the parallax is given in milliarcseconds.

In Figure 28, the form of the CMD of the sample is compared with and without the aforementioned restriction on the parallax uncertainty. As can be seen, the typical features of a HRD, such as the giant branch and horizontal branch, are much more clearly defined in Figure 28b, as the scatter is reduced, and an implausibly high number of bright objects beyond $M_G = -5$ are removed. Note that in Figure 28, the colours have not yet been dereddened. Figure 29 depicts the dereddened CMD of 10205 objects, where $(BP - RP)_0$ was determined as described above. This introduces a large scatter, especially visible in the giant branch, because of the large variance around the transformation curve depicted in Figure 27. Other reasons are measurement uncertainties and cosmic scatter, for example that the metallicity of a star has an effect on its colour. The vertical line structure is a result of $(B - V)_0$, used to calculate $(BP - RP)_0$, being given to two decimal places only.

Now, stellar isochrones are plotted into the colour-magnitude diagrams. Stellar isochrones are curves along which the age of stars is equal. An example of their application is the determination of ages of open clusters by com-

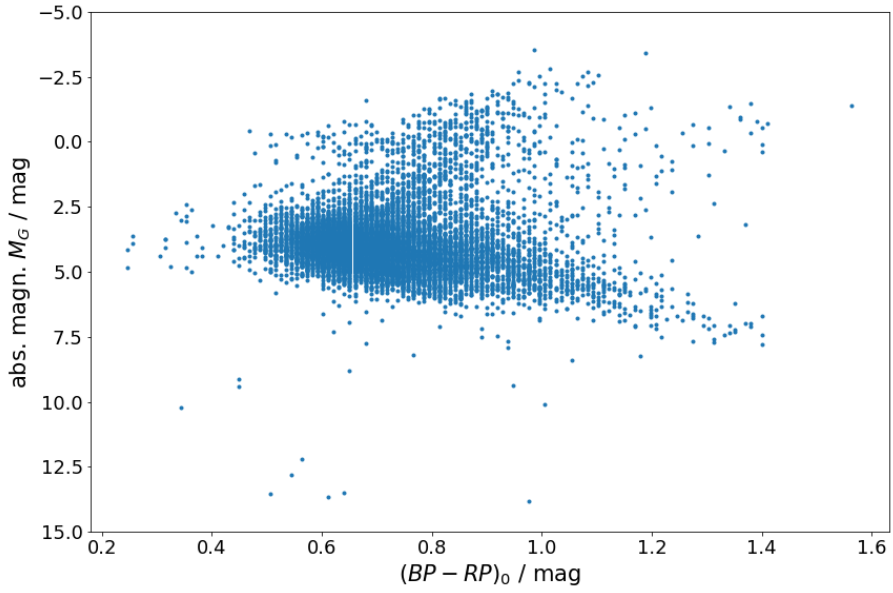


Figure 29: Dereddened CMD of the 10205 objects from the Christlieb et al. (2008) sample left after crossmatching and applying parallax conditions.

puting several isochrones of different ages and metallicities from the open clusters' initial mass function and checking which age fits best for an appropriate metallicity. In general, the position of the main sequence turnoff and isochrones depends on the metallicities (Frebel 2015): since many metal lines are in the blue spectral range, the opacity in the blue spectral range in metal-poor stars is much lower than the opacity in the blue spectral range in stars of higher metallicity, meaning isochrones representing lower metallicities are shifted further towards blue. In this work, the PARSEC isochrones (Bressan et al. 2012) are used, which are available for the metallicity range $-2.2 \leq [M/H] \leq +0.5$.

Several isochrones of the age 12 Gyr are computed for the Gaia photometric system using the PARSEC web interface⁶. They are depicted within the CMD in Figure 30. Strictly speaking, plotting the isochrones only makes sense in a dereddened CMD, i.e. Figure 30b. However, Figure 30a is still produced to compare to Figure 30b: while before dereddening, the giant branch lies mainly in the range between $[M/H] = -1.0$ and $[M/H] = -1.6$, in the dereddened CMD it has moved beyond the $[M/H] = -2.0$ isochrone, indicating an even lower metallicity for many of the stars.

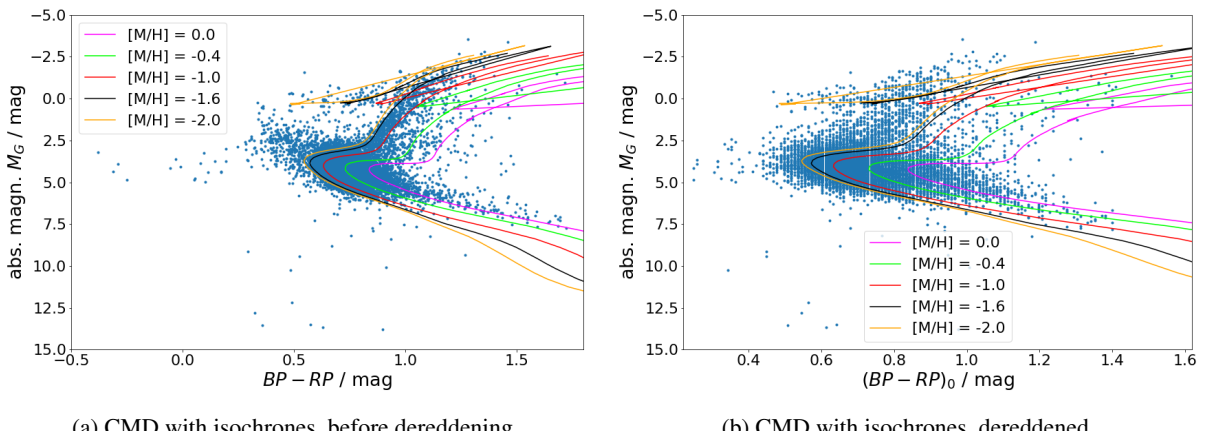
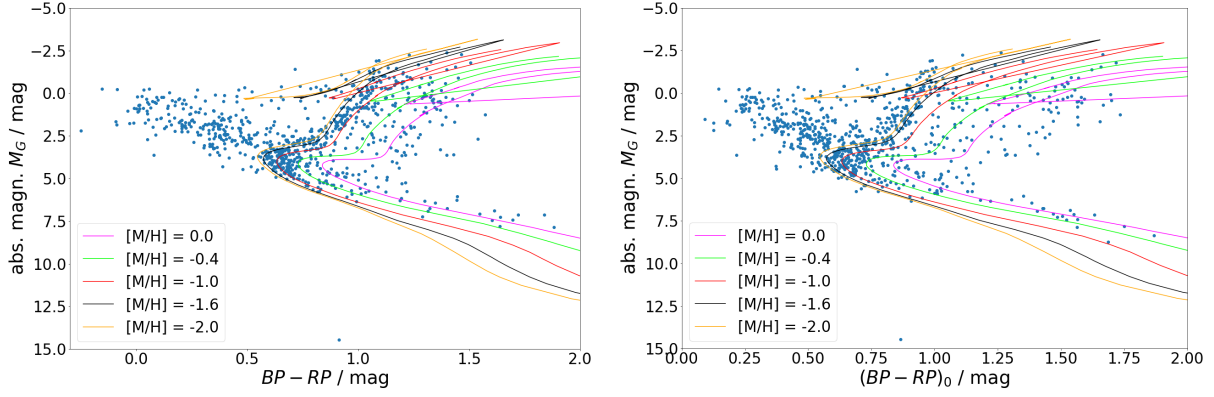


Figure 30: CMDs of the Christlieb et al. (2008) sample including isochrones.

⁶<http://stev.oapd.inaf.it/cgi-bin/cmd>, retrieved 30.07.2020

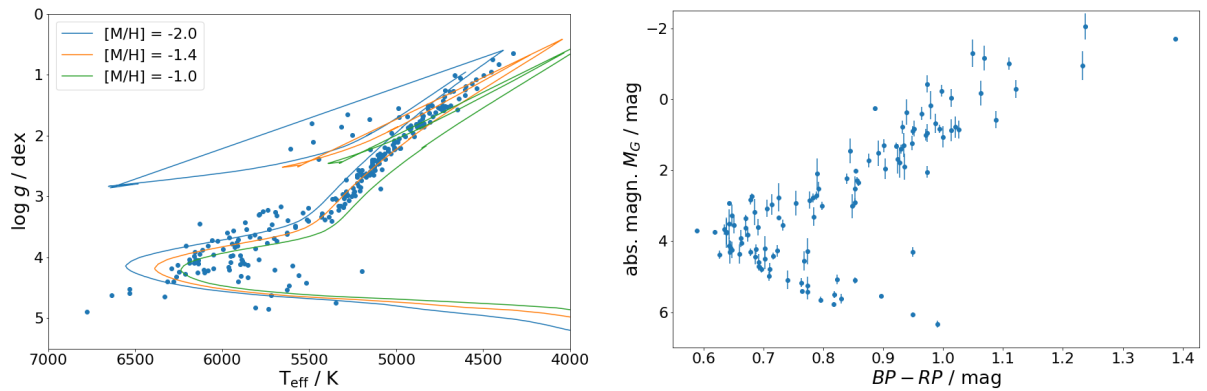


(a) CMD with isochrones, before dereddening.

(b) CMD with isochrones, dereddened.

Figure 31: CMDs of the Beers et al. (2007) sample including isochrones.

The same procedure as for the Christlieb et al. (2008) sample is carried out for the Beers et al. (2007) sample: the dereddened colour $(BP - RP)_0$ is determined from $(B - V)_0$ and the transformation (26), A_G is computed according to (27) and (28), the parallaxes are restricted to a relative precision of 20% and the same isochrones as before are used. Here, the crossmatch and parallax conditions reduce the number of usable objects to only 824. The resulting CMDs are in line with the CMDs created before, as shown in Figure 31: Once again, the reddening moves the sample in a metallicity range of -2.0 or lower, as seen in Figure 31b. More so for this sample than the previous one, it can be observed that the cool main sequence stars appear to have solar or near-solar metallicities, which is expected, since they are most likely foreground stars of the Galactic disc population. Also, it can be observed that of the stars in the sample that were selected as candidate FHB/A stars, quite a lot of are in fact on the main sequence and not part of the horizontal branch, even though Christlieb et al. (2005) report a contamination of HES FHB candidates by main sequence A-type stars of only up to 16 %. The comparatively large number of main sequence stars could be due to the fact that only 125 of the 576 FHB/A candidates in the sample were taken from the FHB candidate sample by Christlieb et al. (2005). Additionally, only 824 objects of the initial 1857 are left in Figure 31, so it is likely that many FHB stars were cut as a result of the crossmatch and the parallax conditions.



(a) Kiel diagram of the Barklem et al. (2005) sample. Uncertainties in $\log g$ and T_{eff} were left out for better visibility.

(b) CMD of the sample, with the uncertainty in absolute magnitude included.

Figure 32: Kiel diagram and CMD of the Barklem et al. (2005) sample.

In Figure 32a, the sample of Barklem et al. (2005) is depicted, plotting the surface gravity against the effective temperature given by them in a so-called Kiel diagram. This sample is used to demonstrate the scale of the uncertainty of the absolute magnitude, as the lower number of objects improves the visibility of the errorbars. A CMD is produced analogously to before, leaving 125 objects after the parallax condition. The uncertainty can be

estimated as

$$\Delta M_G = \sqrt{(\Delta G)^2 + \left(\frac{5\Delta\varpi}{\ln(10)\varpi} \right)^2}, \quad (30)$$

where the uncertainty of the G magnitude ΔG is given by Gaia Collaboration, Brown et al. (2018) as approximately 0.3 mmag at $G < 13$ mag, 2 mmag at $G = 17$ mag and 10 mmag at $G = 20$ mag. The extinction in the G band, A_G , was not taken into account. However, the parallax uncertainty generally dominates; in fact, even including the G magnitude uncertainty is somewhat unnecessary, as it turned out to not really make much of a difference in the presence of the parallax uncertainty. In Figure 32b, the CMD of the sample is shown with errorbars. A slight trend of brighter stars (absolute magnitude) having larger uncertainties more often can be observed.

4.3 Selection and follow-up spectra

Using the Christlieb et al. (2008) sample, a region of the diagram is selected using a cutoff line, as depicted in Figure 33. The cutoff line is defined with the intention of including objects below the main sequence as well as those furthest on the blue end. The specific linear equations describing the two straights making up the cutoff line are

$$y = 4x + 2.93 \quad \text{and} \quad (31)$$

$$y = 20x - 5.07 \quad (32)$$

for the right and left lines, respectively, where y corresponds to the absolute magnitude axis and x to the colour axis. The number of objects below the cutoff line is 126, marked red in Figure 33.

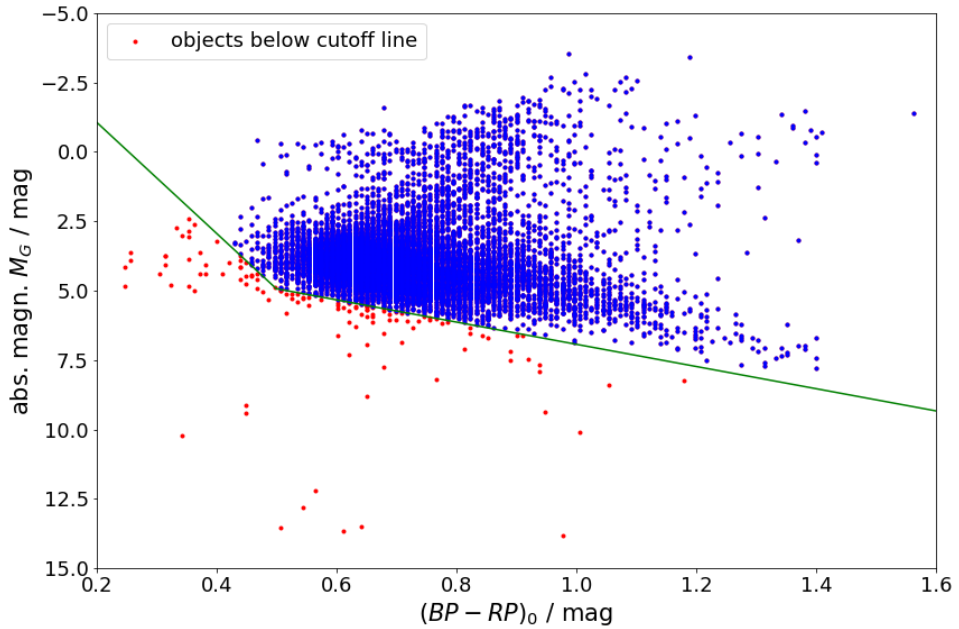


Figure 33: The cutoff lines applied to the first sample.

All 126 objects are searched for in the SIMBAD Astronomical Database⁷ provided by the CDS, using the coordinates of the objects. Of the 126 objects, most are currently not part of the SIMBAD database, however, 3 objects are identified as white dwarfs and 16 as hot subdwarfs.

Hot subdwarfs are stars that have evolved beyond the main sequence and are found at the blue end of the horizontal branch and even beyond within a Hertzsprung–Russell diagram, being located between the white dwarf region and the very hot end of the main sequence. They burn helium in their core and are classified into two subtypes: B-type

⁷<http://simbad.u-strasbg.fr/simbad/>, retrieved 30.07.2020

Star	α (J2015.5)	δ (J2015.5)	G [mag]	T_{eff} [K]	Gaia ID	2MASS ID
(1) HE 0233+0105	02 35 51.3	+01 18 44.9	16.2	6919 $^{+293}_{-241}$	2502097283492466560	J02355136+0118452
(2) HE 0851+0148	08 54 22.4	+01 36 50.7	16.0	9613 $^{+127}_{-1321}$	577615106369494528	J08542239+0136509
(3) HE 1333-0622	13 36 19.6	-06 37 58.5	16.0	7176 $^{+1264}_{-270}$	3630940995279668096	J13361963-0637584

Table 2: White dwarfs found in SIMBAD.

Star	α (J2015.5)	δ (J2015.5)	G [mag]	T_{eff} [K]	Gaia ID	2MASS ID
(a) HE 0003-3509	00 05 56.7	-34 53 06.6	15.2	9566 $^{+146}_{-519}$	2309702230603610112	J00055671-3453066
(b) HE 0154-1409	01 56 31.9	-13 54 28.2	12.3	8869 $^{+724}_{-905}$	5149241067178231552	J01563189-1354263
(c) HE 0239-2038	02 41 19.9	-20 25 57.5	15.3	8690 $^{+431}_{-421}$	5127043031220599936	
(d) HE 0410-4901	04 11 30.2	-48 53 47.7	14.5	8869 $^{+724}_{-905}$	4830756636452153984	J04113017-4853478
(e) HE 0422-2802	04 24 46.7	-27 55 12.1	15.9	8858 $^{+331}_{-467}$	4892094060839586688	
(f) HE 0430-2457	04 33 03.8	-24 51 19.7	14.2	9517 $^{+181}_{-1969}$	4894595552871931008	
(g) HE 1221-2618	12 24 32.7	-26 35 16.7	14.6	8865 $^{+324}_{-499}$	3476266612927121536	J12243266-2635165
(h) HE 1133-1638	11 36 03.5	-16 54 56.9	14.8	9566 $^{+189}_{-2018}$	3547913225838503808	J11360348-1654567
(i) HE 1135-2850	11 38 28.8	-29 06 55.2	15.1	9168 $^{+382}_{-579}$	3483602210912236416	J11382877-2906550
(j) HE 1309-0749	13 11 45.0	-08 05 22.3	14.0	9579 $^{+162}_{-526}$	3628235887437668480	J13114497-0805216
(k) HE 1441-0558	14 44 12.1	-06 10 44.8	14.3	9593 $^{+125}_{-1301}$	6336921024852699648	J14441210-0610447
(l) HE 1459-0234	15 02 12.1	-02 45 58.0	14.8	8630 $^{+538}_{-559}$	6339679321569685504	J15021213-0245577
(m) HE 2156-3927	21 59 35.5	-39 13 14.9	14.4	8869 $^{+724}_{-905}$	6574414299502733824	J21593550-3913150
(n) HE 2202-3534	22 05 48.2	-35 19 38.8	13.2	9365 $^{+248}_{-2819}$	6587335519633433472	J22054816-3519386
(o) HE 2213-2212	22 16 23.5	-21 57 26.1	13.9	8552 $^{+1061}_{-3754}$	6819214275593537920	
(p) HE 2342-1545	23 45 26.7	-15 28 38.6	15.7	9519 $^{+185}_{-829}$	2418838380386828672	J23452669-1528386

Table 3: Hot subdwarfs found in SIMBAD.

subdwarfs (sdB), which are spectroscopically homogeneous and are mostly helium-poor, and O-type subdwarfs, usually post-red-giant branch, post-horizontal branch or post-asymptotic giant branch stars with widely varying spectra. Generally, low-mass stars become hot subdwarfs at a late point in their evolution. The spectral features of an sdB star include very broad Balmer lines, considering they belong to the spectral class B, when compared to corresponding main sequence stars, while for some sdB stars, HeI lines are weak for their colour. In sdO stars, HeII lines are observed and they are usually classified as either H strong-lined or He strong-lined sdO stars (Heber 2009).

The objects found in SIMBAD are listed in Table 2 and Table 3. The coordinates right ascension α and declination δ are taken from Gaia DR2 (ICRS, epoch J2015.5), as are the magnitude in the G band and the effective temperature T_{eff} . Additionally, 2MASS identifiers are also included when listed in SIMBAD. The G magnitude is rounded to 1 digit while for the effective temperature, digits behind the decimal point were omitted.

Figure 34 shows the positions of all objects listed in Table 2 and 3 in the CMD. All the hot subdwarfs occupy the region on the blue end of the CMD to the left of the main sequence turnoff, where they are expected. However, the effective temperatures of the objects reported in Gaia DR2 (see Table 3) appear rather low for B-type stars (let alone O-type). This is because the temperature range in Gaia DR2 is limited to 3000 K to 10 000 K, due to there not having been enough literature estimates outside that range to obtain good results. The machine learning algorithm used does not extrapolate and the temperatures of stars beyond 10 000 K is erroneously put into the range mentioned above (Andrae et al. 2018). This is likely also the reason for the T_{eff} values of (b), (d) and (m) in Table 3 being equal even down to their uncertainty estimates. This unreliability of effective temperatures in Gaia DR2 outside a certain range should be kept in mind continuing on. Of the three white dwarfs found in SIMBAD, the position of two of them is plausible, while one of them is among the hot subdwarfs. This star is classified by Kepler et al. (2015) as a PG1159 star, which is a star in transition between the hottest post-asymptotic giant branch stage and the white dwarf stage (Hügelmeyer et al. 2007), explaining this unexpected position in the CMD.

Finally, some spectra of objects below the cutoff line that were available are qualitatively investigated. In the appendix A, ten objects' spectra along with their position in the CMD and some additional parameters are shown. Position and effective temperature are taken directly from Gaia DR2, while the colour's and absolute magnitude's

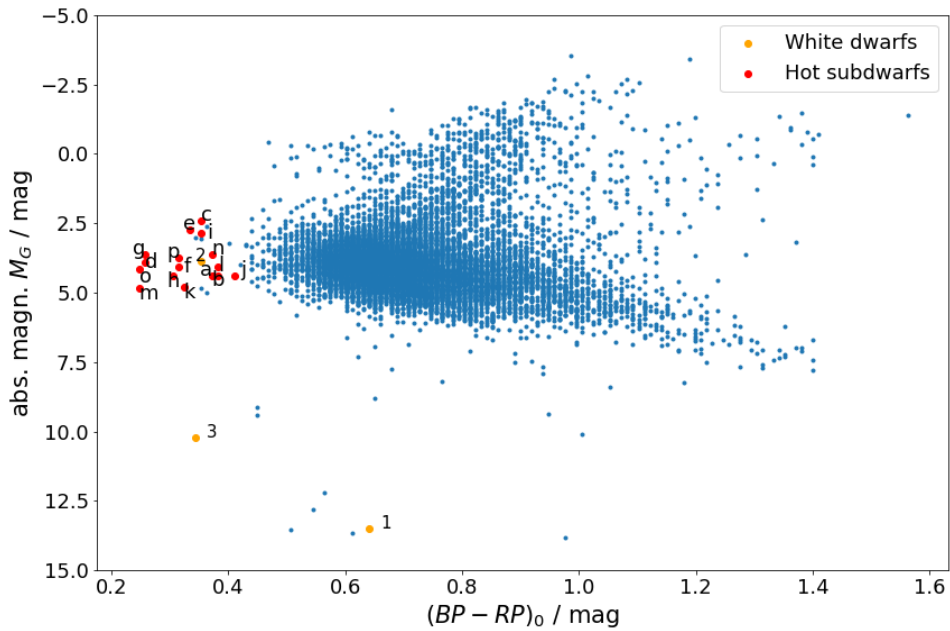


Figure 34: The hot subdwarfs and white dwarfs according to SIMBAD.

derivation was already described in the previous section. The line indices and metallicity estimates came with the sample (Christlieb et al. 2008) and the distance estimate is taken from Bailer-Jones et al. (2018).

HE 0205-2434 The Balmer lines (4861 Å, 4340 Å, 4102 Å, 3970 Å, 3889 Å, 3835 Å, ...) are strong, as are the calcium H+K lines (3968 Å+3934 Å). The CH G band at \sim 4300 Å is clearly visible. Since the object is close to the main sequence, this is probably a main sequence star of spectral type F, with which the effective temperature is also in agreement.

HE 0219-3312 The spectral energy distribution indicates a rather cool star (which the Gaia DR2 effective temperature confirms) with notably smaller flux in the blue range. The wobbly character of the spectrum is likely not due to a low signal-to-noise ratio, but due to strong absorption bands, e.g. titanium bands at 4500~4750 Å. Notably, the calcium H and K lines are in emission. Although it is somewhat far from the main sequence, it could be a dKe dwarf.

HE 0233+0105 The Balmer lines hint at the star being fairly hot. The calcium K line is weak, while the calcium H line is dominated by the He line at \sim 3970 Å. The small, shallow Balmer jump suggests that this star could be a cool DA white dwarf (which are usually hotter). The position in the CMD puts the star firmly into the white dwarf region.

HE 0513-2355 This star is rather cool (which the Gaia DR2 concurs with), with weak Balmer lines. The calcium H+K lines, however, are pretty strong. From its spectrum, it would be expected close to the main sequence, but the CMD reveals its location somewhat below the main sequence.

HE 1243+0201 Due to the given excerpt being so small, not much information can be obtained about the spectral energy distribution. The calcium H+K lines appear fairly pronounced and the Balmer lines are also visible. The CMD puts it just below the main sequence.

HE 1347-2607 The Balmer lines are quite broad and the CH G band is visible. The Balmer jump is weak. It could be a cool white dwarf.

HE 1441-0558 The spectral energy distribution indicates a very blue star, the Balmer lines are rather strong, and helium lines are present (e.g. Hel at \sim 4471 Å). This indicates a hot subdwarf, which the position of the star in

the CMD confirms.

HE 2122-4237 The lack of any clearly visible absorption lines implies that this star is a DC white dwarf. Its location in the CMD places it in the cold range of the white dwarf region.

HE 2328-1646 & HE 2343-2307⁸ These stars appear to be normal, relatively metal-poor F- or G-type stars near the main sequence turnoff. The calcium H+K lines are highly visible, as are some Balmer lines.

4.4 Comparison of stellar parameters

4.4.1 Effective temperature

In order to detect possible systematic differences between the effective temperatures determined by Barklem et al. (2005) for their sample of 253 stars (from the Alonso et al. (1999) colour calibrations) and the effective temperatures given in Gaia DR2, which were determined using a machine learning algorithm on Gaia photometric data (see Andrae et al. 2018), the Gaia effective temperature is plotted against the Barklem effective temperature (Figure 35a). Barklem et al. (2005) estimated the uncertainty of their results as ~ 100 K, while in Gaia DR2, an upper and lower uncertainty limit for the effective temperature is given. A figure depicting these errorbars is also produced (Figure 35b). The yellow line in the figures represents the identity relation.

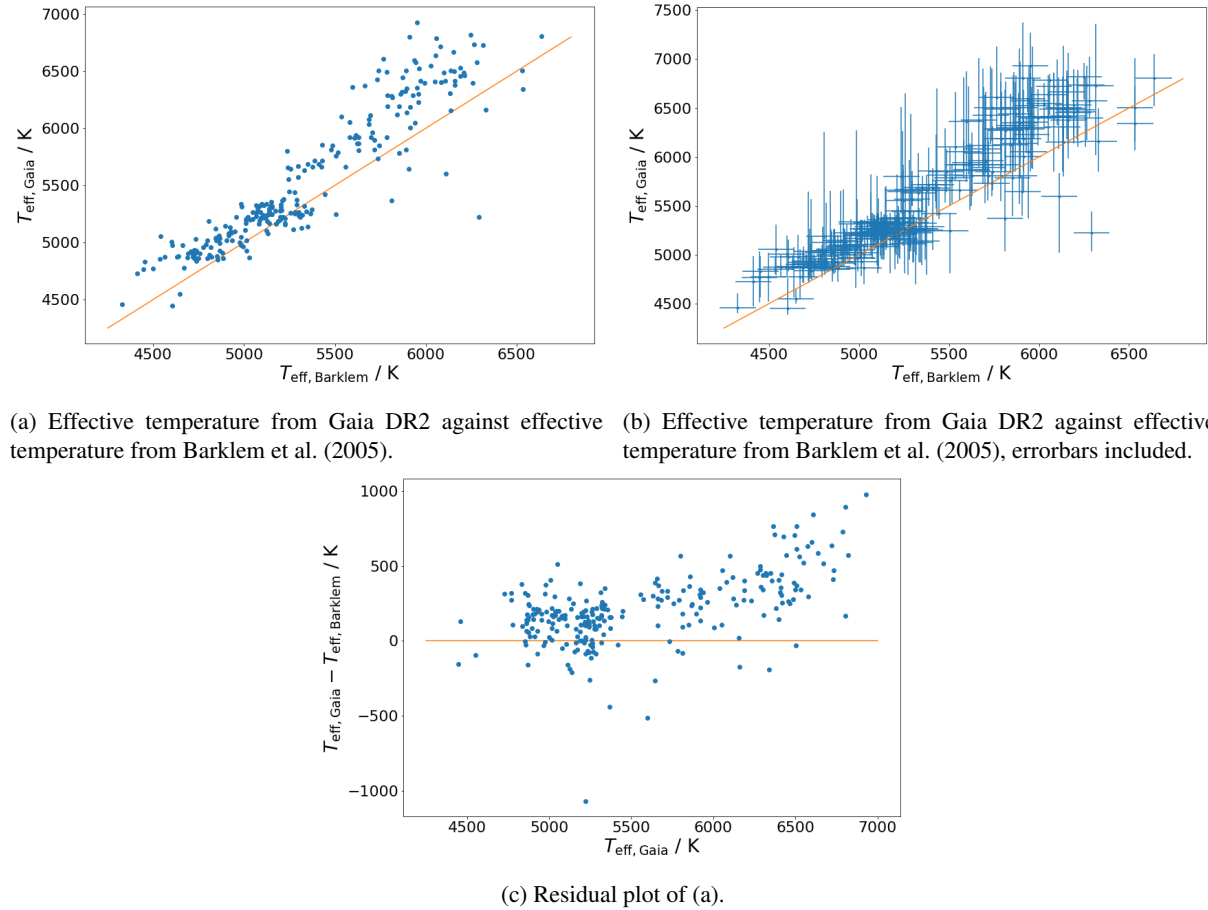


Figure 35: Comparison of effective temperatures between Gaia DR2 and Barklem et al. (2005).

⁸These final two stars are not in fact part of the sample selected using the cutoff line in Figure 33, but are slightly above the line, as seen from the positions in the CMD. They were selected by the cutoff line used in the CMD before dereddening at an earlier stage of working on this thesis, and were now included so the number of examined spectra does not become too small.

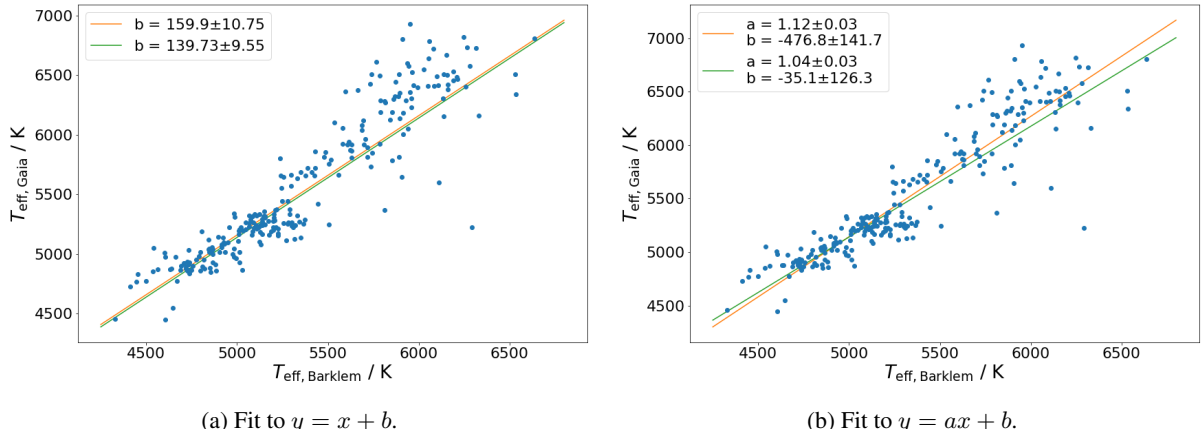


Figure 36: Linear fits between the temperatures.

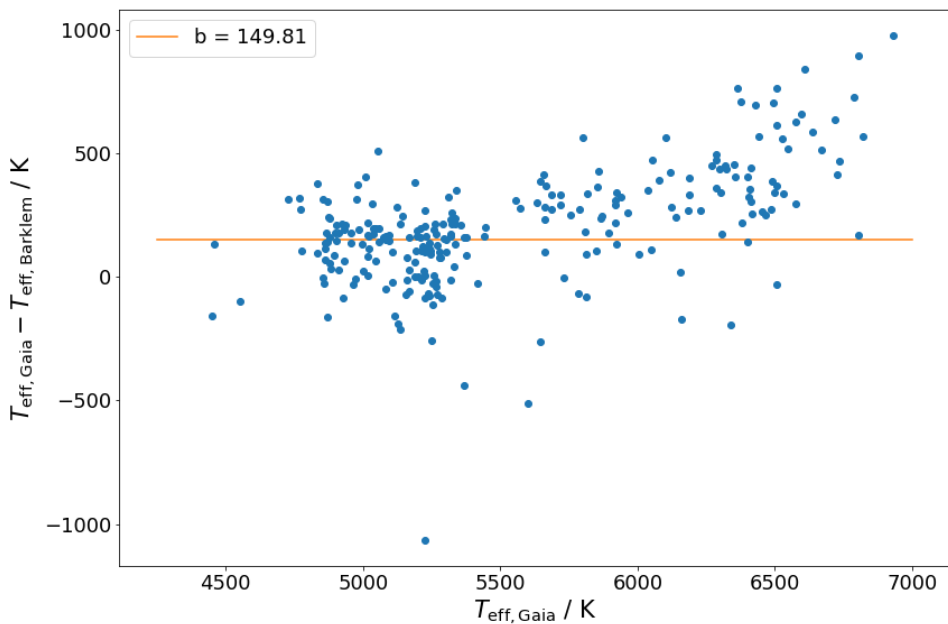
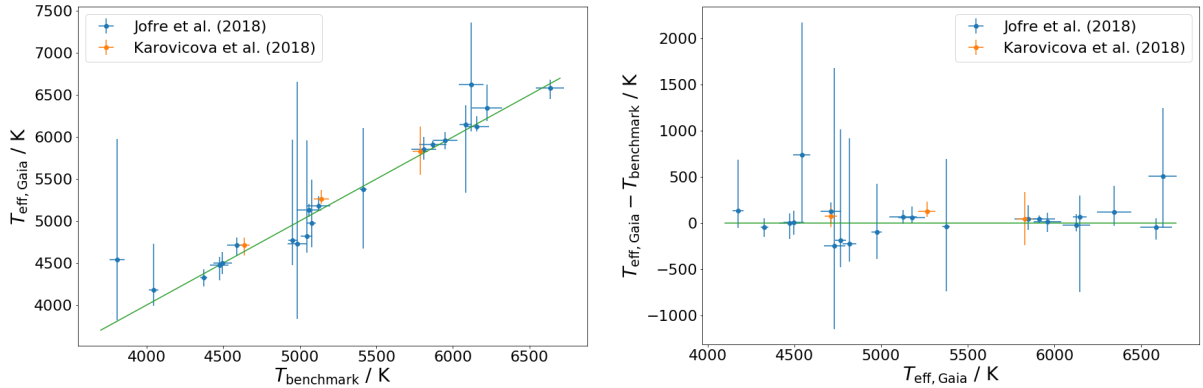


Figure 37: Residual plot of temperatures, offset 149.8 K indicated by yellow line.

Figure 35c depicts the difference between the two temperature estimates plotted against the Gaia DR2 temperature. As can be seen, there's a systematic offset, with the Gaia DR2 temperature being systematically higher. Towards the hot end, the deviation grows larger as does the scatter in general. To quantify the deviation, two linear least squares fits $y = ax + b$ are carried out: one where both a and b are fit parameters, and one where $a = 1$ is set. Since for Gaia DR2, the uncertainties above and below the temperature differ, for each of the two cases again two fits are done, giving an upper and lower estimate for the fit parameters. The fits are shown in Figure 36.

From Figure 36a, the systematic offset between Gaia DR2 and Barklem data is estimated by taking the arithmetic mean of the upper and lower fit, yielding (149.8 ± 7.2) K as the offset by which the Gaia DR2 temperatures lie above the Barklem temperatures. As shown in the residual plot in Figure 37, this offset works well for objects at lower temperatures of up to ~ 5500 K; from there on, however, the deviation of objects increases. This also means that the actual offset of the objects at lower temperatures is lower than 149.8 K, with the objects at higher temperatures boosting the fit parameter b .

The growing scatter and deviation of stars at higher temperatures could be explained by the extrapolation range of the Barklem stars. In Table 6 of Alonso et al. (1999), several broadband colours and their corresponding effec-



(a) Gaia DR2 effective temperature against benchmark stars
(b) The difference between the effective temperatures as a function of the Gaia effective temperature.

Figure 38: Comparison of effective temperatures between Gaia DR2 and the benchmark stars.

tive temperatures are listed for the metallicities $[Fe/H] = -1.0$, $[Fe/H] = -2.0$ and $[Fe/H] = -3.0$, which is the range of the sample investigated. Table 6 reveals that their relation between colour and effective temperature becomes increasingly unreliable, or is mostly not available at all, at higher temperatures (and lower metallicities). For instance, even at $T_{\text{eff}} = 5750$ K for $[Fe/H] = -2.0$, reliable relations are given for only half of the broadband colours. Since Barklem et al. (2005) obtained their temperature estimates from Alonso et al. (1999), this could explain the deviations observed.

Lastly, the Gaia effective temperatures are compared to 35 benchmark stars whose effective temperatures were determined to a high degree of accuracy by Jofre et al. (2018), as well as HD140283, HD122563 and HD103095, whose effective temperatures were accurately determined by Karovicova et al. (2018). During the crossmatch procedure, only 25 of the 35 stars could be identified and for 4 more, no effective temperatures were given for the benchmark stars or in Gaia DR2, leaving only 21 for the comparison, which however suffices for this purpose. The three Karovicova et al. (2018) stars were identified manually.

Figure 38 shows that most stars are located quite closely along the identity, aside from a few exceptions, which reinforces the Gaia DR2 effective temperatures in this range. The errorbars of the exceptions are so large that the corresponding benchmark effective temperatures are still within their uncertainty limits.

4.4.2 Surface gravity

Finally, the surface gravities determined for the sample of 253 stars by Barklem et al. (2005) are compared to the surface gravities derived from Gaia DR2 data. While the former were determined in an automated spectrum analysis, the latter can be determined using

$$\log \varpi = 0.5 \log \frac{g}{g_{\odot}} - 0.5 \log \frac{M}{M_{\odot}} - 2 \log \frac{T_{\text{eff}}}{T_{\text{eff}\odot}} - 0.2(V + BC - A_V + 5 - M_{\text{bol}\odot}), \quad (33)$$

where ϖ refers to the spectroscopic parallax, g to the surface gravity, M to the mass, T_{eff} to the effective temperature, V to the Johnson-Cousins V band magnitude, BC to the bolometric correction and A_V to the extinction in the V band for the star. $M_{\text{bol}\odot}$ refers to the bolometric magnitude of the Sun and g_{\odot} , M_{\odot} as well as $T_{\text{eff}\odot}$ to the aforementioned quantities, but for the Sun. The formula is taken from Perryman (2008) with a slight change, as there was a small error. Transforming equation (33), the surface gravity is

$$\log g = 2 \log \varpi + \log g_{\odot} + \log \frac{M}{M_{\odot}} + 4 \log \frac{T_{\text{eff}}}{T_{\text{eff}\odot}} + 0.4(V + BC - A_V + 5 - M_{\text{bol}\odot}). \quad (34)$$

Since for the derivation of the surface gravity $\log g$, parallax data from Gaia is needed, the 20 % relative uncertainty condition is once again imposed on the sample, leaving only 125 stars for the following analysis. The effective temperatures T_{eff} in equation (34) are taken directly from Gaia DR2, as is the parallax ϖ , even though there is a difference between geometric and spectroscopic parallax, thus constituting a possible error source. The

V magnitude is once again determined according to equation (21), while the A_V extinction is calculated from $A_V = 3.1 \cdot E(B - V)$ (Schultz & Wiemer 1975), with $E(B - V)$ taken from the Schlegel et al. (1998) maps. The surface gravity $g_\odot = 274 \text{ m/s}^2$ and effective temperature $T_{\text{eff}\odot} = 5772 \text{ K}$ are taken from the Sun Fact Sheet⁹ by NASA.

To determine the masses of the objects, a PARSEC isochrone of metallicity $[\text{M}/\text{H}] = -2.0$ is used, where $[\text{M}/\text{H}] = -2.0$ is chosen because the sample consists of metal-poor stars. Since each point on the isochrone is also associated with a mass (which is part of the output table for PARSEC isochrones), the approach is to take the nearest point on the curve for each object in the CMD and assign the corresponding mass to it. Since the absolute magnitudes and colours are only known down to a certain accuracy, the error ellipsis around each object also has to be taken into account. The CMD with the isochrone and error ellipses is shown in Figure 39.

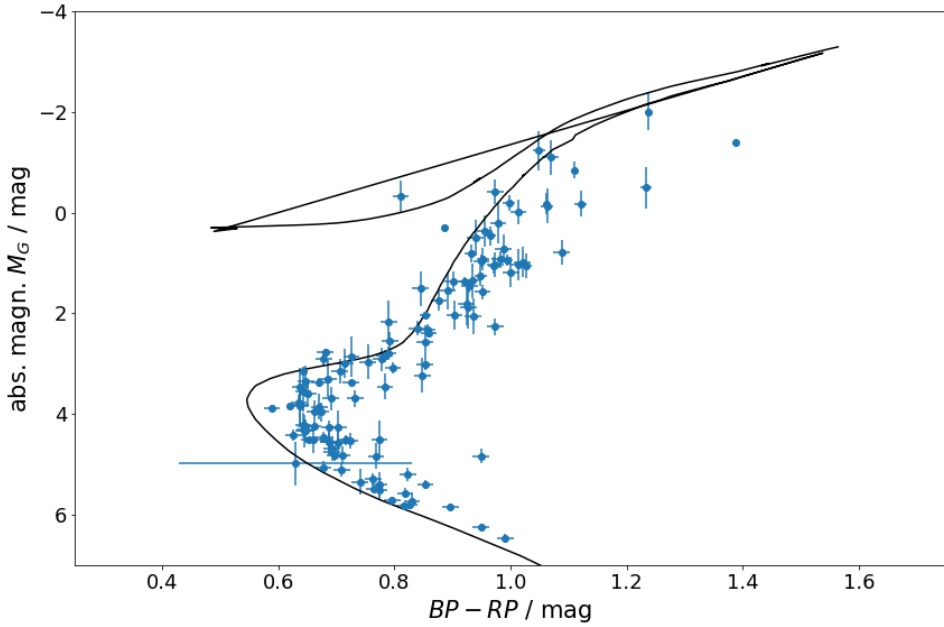


Figure 39: Barklem et al. (2005) sample with an isochrone (age 12 Gyr, metallicity $[\text{M}/\text{H}] = -2.0$). The mass of each object is determined by comparing its position in the CMD with the isochrone.

Specifically, the distance δ_i between an object and each point i of the isochrone, normalised to the errors σ_{BP-RP} and σ_{M_G} , is given by

$$\delta_i = \sqrt{\frac{\{\Delta(BP - RP)\}_i^2}{\sigma_{BP-RP}^2} + \frac{\{\Delta M_G\}_i^2}{\sigma_{M_G}^2}}. \quad (35)$$

The smallest δ_i is chosen and the mass associated with it is assigned to the object. In Gaia Collaboration, Brown et al. (2018), the uncertainty in the G band is approximated as 0.3 mmag for $G < 13$ mag, 2 mmag at $G = 17$ mag and 10 mmag at $G = 20$ mag, while the BP and RP band uncertainties are 2 mmag at $G < 13$ mag, 10 mmag at $G = 17$ mag and 200 mmag at $G = 20$ mag. For $BP - RP$, the error thus becomes

$$\sigma_{BP-RP} = \sqrt{(\Delta BP)^2 + (\Delta RP)^2}, \quad (36)$$

while for M_G , the error is given by

$$\sigma_{M_G} = \sqrt{(\Delta G)^2 + \left(\frac{5}{\varpi \ln 10} \Delta \varpi \right)^2}, \quad (37)$$

where $\Delta \varpi$ is the parallax error. The PARSEC isochrones' mass data is already given in units of the solar mass, M/M_\odot .

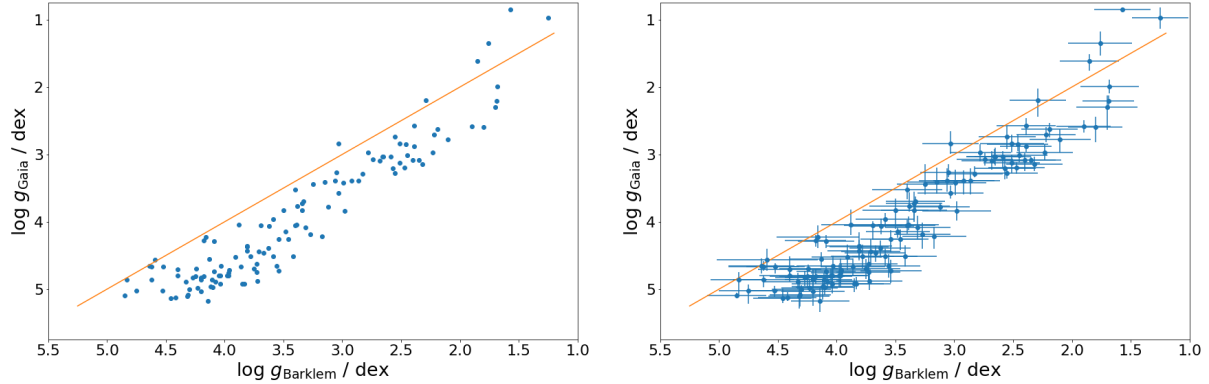
⁹<https://nssdc.gsfc.nasa.gov/planetary/factsheet/sunfact.html>, retrieved 30.07.2020

The bolometric corrections are calculated following Torres (2010), which is based on Flower (1996), expressing it as a function of T_{eff} ,

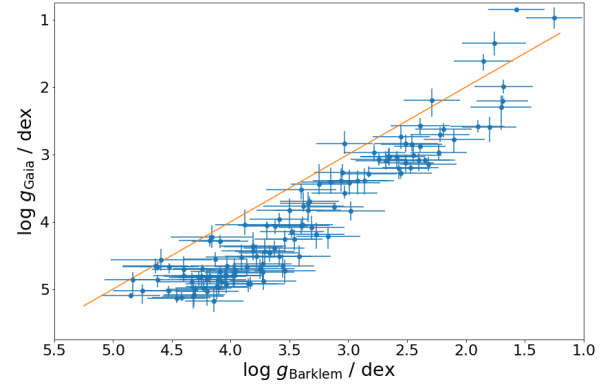
$$\text{BC} = a_1 + b_1(\log T_{\text{eff}}) + c_1(\log T_{\text{eff}})^2 + d_1(\log T_{\text{eff}})^3 \quad \text{and} \quad (38)$$

$$\text{BC} = a_2 + b_2(\log T_{\text{eff}}) + c_2(\log T_{\text{eff}})^2 + d_2(\log T_{\text{eff}})^3 + e_2(\log T_{\text{eff}})^4, \quad (39)$$

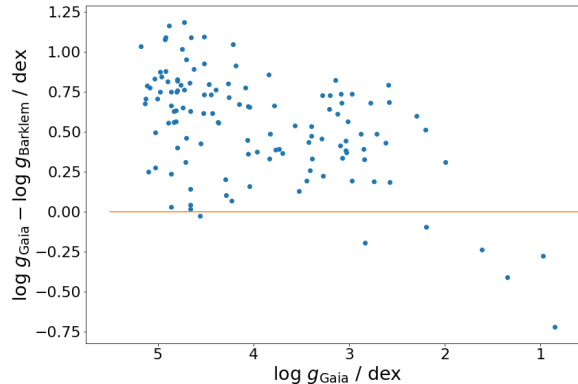
for $\log T_{\text{eff}} < 3.70$ and $3.70 < \log T_{\text{eff}} < 3.9$, respectively. The coefficients can be found in Torres (2010), as can the bolometric magnitude of the Sun, $M_{\text{bol}\odot} = 4.81$, used in equation (34). For the effective temperature, the Gaia DR2 temperatures were taken. With all parameters finally assembled, $\log g$ can be determined for all objects. The surface gravity given by Barklem et al. (2005) is plotted against the surface gravity determined from Gaia data as described above for each object (Figure 40a).



(a) Surface gravity from Gaia DR2 against surface gravity from Barklem et al. (2005).



(b) Surface gravity from Gaia DR2 against surface gravity from Barklem et al. (2005), errorbars included.



(c) Residual plot of (a).

Figure 40: Comparison of surface gravities between Gaia DR2 and Barklem et al. (2005).

Taking into account the errors of the effective temperatures and parallaxes, the error of the surface gravities can be estimated as

$$\Delta \log g = \frac{2}{\ln 10} \sqrt{\left(\frac{\Delta \varpi}{\varpi} \right)^2 + \left(\frac{\Delta T_{\text{eff}}}{T_{\text{eff}}} \right)^2}. \quad (40)$$

In Figure 40b, errorbars are included. The Gaia $\log g$ errors have probably been underestimated, mostly due to disregarding errors arising from the mass determination as well as the calculation of the V magnitude and the bolometric correction. However, this underestimation is not severe, as the parallax and temperature errors should dominate the other errors. In Figure 40c, a residual plot of the difference between the two surface gravities and the Gaia surface gravity is depicted. In the range higher than $\log g = 2$, a systematic offset is seen, with the Gaia surface gravities being systematically higher, while the few objects below $\log g = 2$ deviate in the other direction.

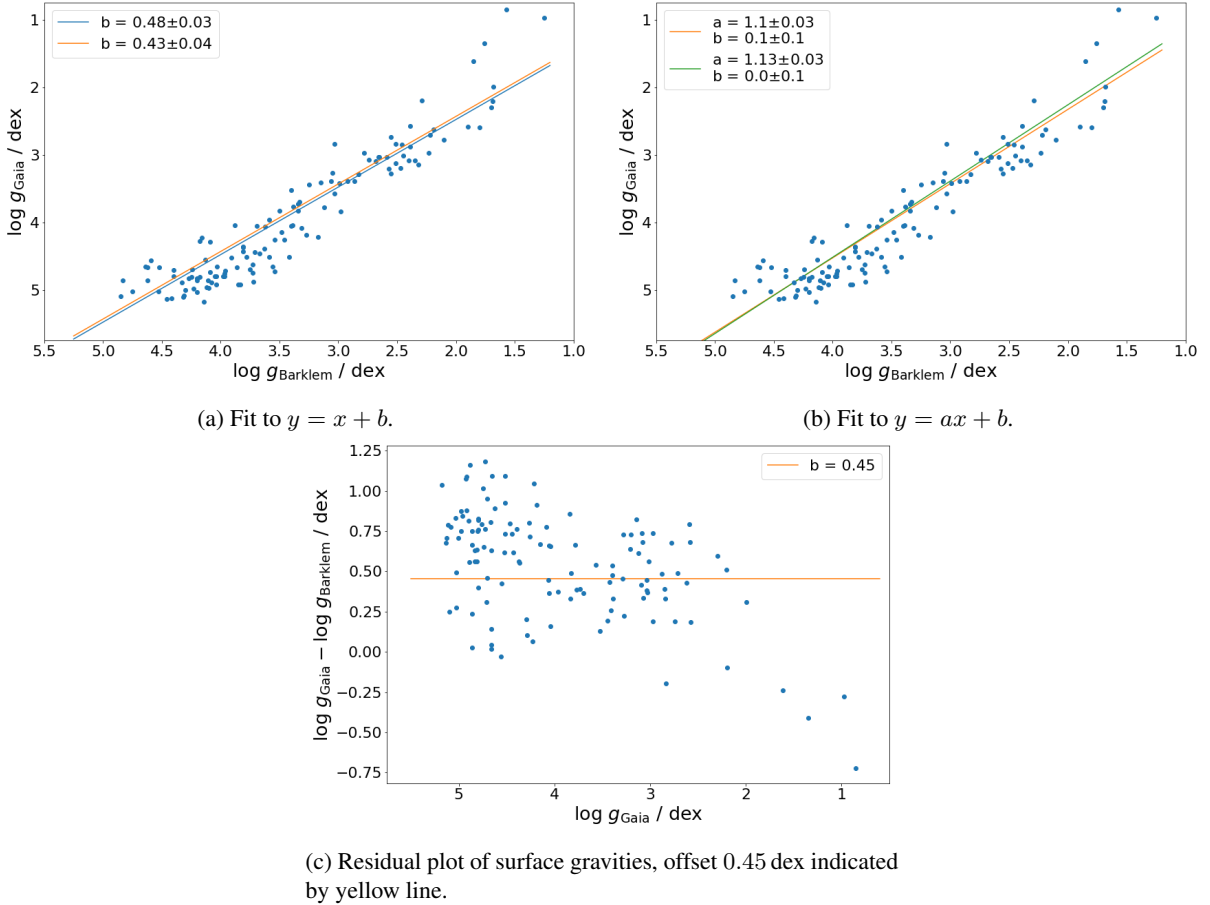


Figure 41: Linear fits between the surface gravities and residual plot including offset line.

However, they are probably not numerous enough to make a statement on a trend. Since the Barklem et al. (2005) surface gravities are based on 1D LTE atmospheric models, NLTE effects contribute to the deviations.

Similarly to Section 4.4.1, two linear fits $y = ax + b$ are carried out, once again one where both the slope and the offset are fit parameters, and one, where a is set equal to 1. Also, the inclusion of the Gaia $\log g$ error again leads to two fits each, as the errorbars are asymmetrical. The results of the fit are presented in Figure 41. From the fit in Figure 41a, the offset between the Gaia surface gravities and Barklem et al. (2005) surface gravities is found to be (0.45 ± 0.02) dex.

5 Results and conclusions

In this section, the results of the previous section are summarised and suggestions for the improvement of some shortcomings are expressed. First, a crossmatch algorithm was implemented for the three samples of Christlieb et al. (2008), Beers et al. (2007) and Barklem et al. (2005), identifying 18373/20271, 1351/1857 and 249/253 objects in Gaia DR2, respectively. Steps 3 and 4 of the algorithm were dropped after the plausibility check already removed all ambiguous assignments. The objects removed in this plausibility check show a bias towards red objects, which were removed much more frequently in comparison (Figure 23). This could be explained by the calibration of Christlieb et al. (2001), where significantly less data points were available in the range above $B - V = 1.0$. The distribution of the angular distances between the Gaia DR2 coordinates and the HES coordinates (Figure 24), as well as the distribution of the absolute proper motion multiplied by the epoch difference between Gaia DR2 and the DSS-I plates (Figure 26), both display maxima well below 3 arcseconds, reinforcing the choice of 3 arcseconds as the search radius of the initial crossmatch. Nevertheless, choosing a larger search radius (and then most likely having to carry out steps 3 and 4 of the algorithm) could yield a higher identification ratio, which is desired, since almost 2000 objects in the Christlieb et al. (2008) sample and about 500 objects in the Beers et al. (2007) sample could not be identified.

Due to the Gaia DR2 extinction being inapplicable to the samples, a transformation between the $B - V$ colour and the $BP - RP$ colour was determined by fitting a linear and quadratic function to the data (Figure 27). Going forward, the linear fit (26) was chosen based on the similarity of the curves in the range where most data points are located. Notably, the deviation of colours around the fitted curve is on the order of 0.3 mag in both directions. The removal of negative parallaxes, as well as parallaxes whose relative uncertainty is more than 20 %, constitutes a truncation of the samples and should usually be avoided, as it may introduce biases (Luri et al. 2018). On top of that, even the 20 % condition is not very strict and may still lead to quantities derived from parallax measurements being biased and suffering from large variances (Bailer-Jones 2015), if the distance is naively assumed as the inverse of the parallax. It is preferable to employ methods of Bayesian inference for the distance estimates. This has been done for the Gaia DR2 catalogue by Bailer-Jones et al. (2018), who estimated the distances to 1.33 billion stars in Gaia DR2, so using these distances instead might have yielded superior results. The dereddening of the CMD (Figure 29) blurred the CMD overall, probably in part owing to the deviations around the colour transformation fit mentioned above. Using alternative reddening estimates, for example from the 3D extinction maps mentioned in Rybizki et al. (2020) or the results of Anders et al. (2019), this could be improved. Plotting in stellar isochrones (Figure 30b), the metallicity of most stars is indicated to be below $[Fe/H] = -2.0$, with which the sample of Beers et al. (2007) (Figure 31b) is also in agreement. The expectation of the cool main sequence stars in the samples being of approximately solar metallicity can also be observed. Finally, the uncertainty in absolute magnitude, which is dominated by the parallax uncertainty, appears to show a slight overall trend of objects with a brighter absolute magnitude having larger uncertainties (Figure 32b), however this can not decisively be settled using the small sample of Barklem et al. (2005).

126 objects were found to be located in the region selected in the dereddened CMD (Figure 33), which was aimed at including the white dwarf region as well as the blue end of the sample. According to SIMBAD, 3 of these are white dwarfs and 16 are hot subdwarfs, all of which were listed along with some information on them in Table 2 and Table 3, respectively, while most objects could not be found in the Simbad database. The position of these 19 objects in the CMD (Figure 34) is consistent with their classification, the one white dwarf found in the hot subdwarf domain most likely being a PG1159 star. The ten spectra of other objects below the cutoff line that were available (see Appendix A) were investigated by eye. All of them were more or less in accordance with their position within the CMD and about half of them appeared to be main sequence stars or stars near the main sequence. For HE 1243+0201, the spectrum does not contain enough information to classify it, while HE 2122-4237 is in all probability a DC white dwarf. HE 1441-0558 is most likely a hot subdwarf, which both the spectrum and its position in the CMD indicate, and HE 1347-2607 and HE 0233+0105 could be a cool white dwarf and a relatively cool DA white dwarf, respectively.

In the last part of the previous section, the effective temperatures and surface gravities of Gaia DR2 and Barklem et al. (2005) were compared. For the effective temperatures (Figure 35a), an offset between both estimates, which amounted to (150 ± 7) K (Figure 37), was found fitting a linear function to the data (Figure 36). For higher temperatures (above ~ 5500 K), the difference between the estimates, as well as the scatter, increase, which could be explained by the Barklem et al. (2005) temperatures becoming increasingly unreliable in that range as a result of

the data from which they were derived being unreliable in that range. A comparison of temperatures of benchmark stars from Jofre et al. (2018) and Karovicova et al. (2018) with Gaia DR2 temperatures (Figure 38) shows that the Gaia DR2 temperature estimates should be relatively accurate in the range depicted.

Lastly, for the surface gravity (Figure 40a), some calculations had to be carried out first. Notably, the mass was determined by fitting an isochrone (age 12 Gyr, metallicity $[M/H] = -2.0$) to the CMD 39. It should be noted that in that particular CMD, the colours were not dereddened due to issues retrieving the Johnson-Cousins colour information of the sample, so a small error in the determination of the masses occurred. The offset between the surface gravities was found to be (0.45 ± 0.02) dex (Figure 41). Almost no data points fall within the range below $\log g = 2.5$ and the data points which are there deviate in the opposing direction to objects between $\log g = 2.5$ and $\log g = 5$, although the number of objects is likely too small to conclusively judge it. Since the Barklem et al. (2005) surface gravities were determined assuming LTE and using a one-dimensional atmosphere model, NLTE effects are likely at play.

6 Outlook

A more complete identification of HES sources in the Gaia DR2 catalogue as well as retaining as many of them as possible throughout the analysis is essential for an improved characterisation of the HES candidate metal-poor stars. Possible approaches to these issues were already hinted at in the previous section. The improvement of the reddening estimates for the Gaia passbands gives further grounds for expanding on some of the work done in this thesis: using the two-dimensional reddening values of the Schlegel et al. (1998) maps is expected to work well only for faraway giants at high galactic latitudes, but not for main sequence stars which are not so far away, since using them implies the assumption that all stars lie beyond all the dust in the Galactic disc. For the latter, calculating a distance dependent partial extinction may be necessary. Alternatively, the photo-astrometric extinctions (and other parameters) determined by Anders et al. (2019) for 265 million Gaia DR2 stars, using the Bayesian StarHorse code and additional photometry from several surveys beside the Gaia survey, are worth considering, since their extinctions and effective temperatures exhibit greater accuracy and precision compared to previous estimates.

Performing detailed error analyses is another task providing interesting insights. For instance, simulations of CMDs could be used to study the expected cosmic scatter in the CMD. By observing how it behaves when quantities such as the distance, metallicity as well as colour and absolute magnitude are varied within their margins of error, the impact of uncertainties in these astrophysical parameters on the form of the CMD can be assessed. An additional point of interest is the statistical characterisation of a flux-limited sample (and also how the statistical character of a distance-limited sample differs from it), which is a metal-poor candidate sample in this case. This characterisation may include, for instance, the ratio between the number of subgiants and main sequence stars, or how many giant stars are included. This could also indicate selection biases in the HES. For this type of task, however, the truncation of the sample as it occurred during the analysis in this thesis must be taken into consideration.

Maíz-Apellániz & Weiler (2018) showed that, although the Gaia photometry is very precise already, some corrections should be applied to the Gaia DR2 photometric data. Including these in the analysis is necessary to reach the best possible results. Finally, the third full data release of the Gaia mission (Gaia DR3), expected in the second half of 2021, will contain not only improved astronomy and photometry¹⁰, but also more precise astrophysical parameters, as discussed by Andrae et al. (2018), and will thus provide the opportunity to improve and extend the analysis carried out in this thesis.

¹⁰<https://www.cosmos.esa.int/web/gaia/release>, retrieved 07.08.2020

Acknowledgements

First and foremost, I would like to mention my advisor Prof. Norbert Christlieb for the time and dedication he put into supervising me. His guidance and support as well as his patience have been invaluable, and I herewith express my deepest gratitude. I would also like to extend my thanks to Theodora Xylakis-Dornbusch for important advice on many occasions and for providing me with a python script, and to PD Dr. Andreas Koch for agreeing to be the secondary examiner. To Adrian Schirra go my thanks for helpful suggestions as well as to other fellow students for often helping me out throughout my studies and sending me study materials I missed.

Additional thanks are due to NASA's Astrophysics Data System (<https://ui.adsabs.harvard.edu/>), which I probably used more than any other website working on this thesis, the DeepL Translator (www.deepl.com/translator), Willy Brandt for introducing BAföG, and the University of Heidelberg for giving me the opportunity to study physics within their facilities.

Last but not least, a debt of gratitude is owed to my friends, who enrich my life in many ways, my father Ulrich for his support, and my mother Nejdie for too many things to name here. Most importantly, I would like to thank my sister Eva for being around and for sticking with me through it all.

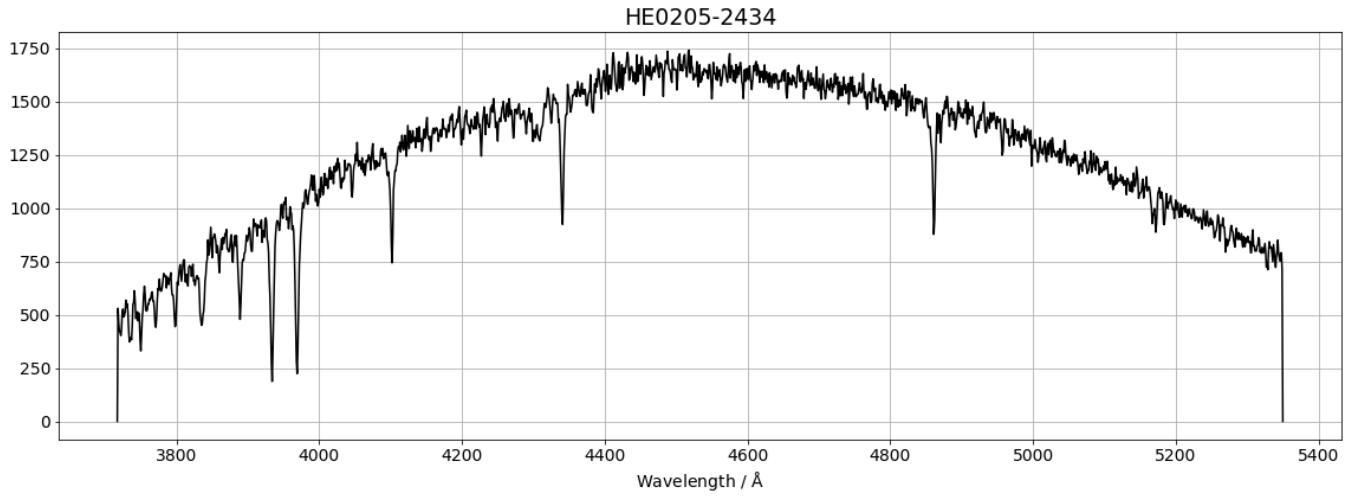
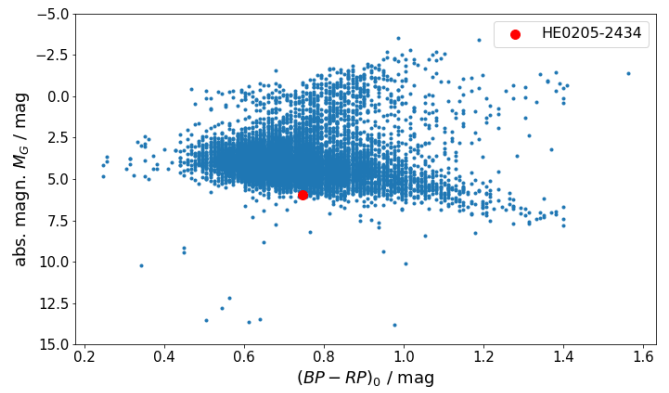
References

- Alonso et al. 1999, A&AS, 140, 261
Anders et al. 2019, A&A, 628, A94
Andrae et al. 2018, A&A, 616, A8
Appenzeller, I. 2013, Introduction to Astronomical Spectroscopy (New York: Cambridge University Press)
Bailer-Jones, C. 2015, PASP, 127, 994
Bailer-Jones et al. 2018, AJ, 156/2, 58
Barklem et al. 2005, A&A, 439, 129
Beers, T. & Christlieb, N. 2005, ARA&A, 43, 531
Beers et al. 1999, AJ, 117/2, 981
Beers et al. 2007, ApJS, 168/1, 128
Bessell, M. 1990, PASP, 102, 1181
Bessell, M. 2005, ARA&A, 43, 293
Bressan et al. 2012, MNRAS, 427, 127
Bromm, V. & Larson, R. 2004, ARA&A, 42, 79
Budding, E. & Demircan, O. 2007, Introduction to Astronomical Photometry, 2nd edn. (Cambridge, UK: Cambridge University Press)
Casagrande, L. & Vandenberg, D. 2014, MNRAS, 444, 392
Christlieb, N. 2000, Dissertation, University of Hamburg
Christlieb et al. 2001, A&A, 366, 898
Christlieb et al. 2005, A&A, 431, 143
Christlieb et al. 2008, A&A, 484, 721
Di Folce et al. 2004, A&A, 426, 601
Evans et al. 2018, A&A, 616, A4
Flower, P. 1996, ApJ, 469, 355
Folkner et al. 1994, A&A, 287, 279
Frebel, A. 2015, Searching for the Oldest Stars: Ancient Relics from the Early Universe (Princeton, New Jersey: Princeton University Press)
Frebel, A. & Norris, J. 2013, Metal-Poor Stars and the Chemical Enrichment of the Universe. In: Planets, Stars and Stellar Systems, 3rd edn. (Dordrecht: Springer)
Frebel, A. & Norris, J. 2015, ARA&A, 53, 631
Freeman, K. & Bland-Hawthorn, J. 2002, ARA&A, 40, 487
Gaia Collaboration, Babusiaux et al. 2018, A&A, 616, A10
Gaia Collaboration, Brown et al. 2018, A&A, 616, A1
Gaia Collaboration, Prusti et al. 2016, A&A, 595, A1
Heber, U. 2009, ARA&A, 47, 211
Herwig, F. 2005, ARA&A, 43, 435
Høg, E. 2014, Asian Journal of Physics, 23
Holl, B. 2012, Characterization and analysis of the astrometric errors in the global astrometric solution for Gaia (Department of Astronomy and Theoretical Physics, Lund University), 6
Hügelmeyer et al. 2007, ASP Conference Series, 372, 249
Jofre et al. 2018, Research Notes of the AAS, 2/3, id.152
Jordi et al. 2010, A&A, 523, A48
Karovicova et al. 2018, MNRAS: Letters, 475/1, 81
Kepler et al. 2015, MNRAS, 446/4, 4078
Kovalevsky, J. 2002, Modern Astrometry, 3rd edn. (Springer), 2
Kovalevsky, J. & Seidelmann, P. 2004, Fundamentals of Astrometry (Cambridge, UK: Cambridge University Press)
Lindegren, L. 2010, Proceedings of the IAU, 261, 296
Lindegren, L. & Bastian, U. 2010, EAS Publications Series, 45, 109
Lindegren et al. 2018, A&A, 616, A2
Luri et al. 2018, A&A, 616, A9
Maíz-Apellániz, J. & Weiler, M. 2018, A&A, 619, A180
Perryman, M. 2008, Astronomical Applications of Astrometry (Cambridge, UK: Cambridge University Press), 343
Perryman, M. 2012, The European Physical Journal H, 37/5, 745
Perryman et al. 2001, A&A, 369, 339
Reimers, D. & Wisotzki, L. 1997, The Messenger, 88, 14
Rybicki et al. 2020, PASP, 132/1013, id.074501
Schlegel et al. 1998, ApJ, 500/2, 525
Schultz, G. & Wiemer, W. 1975, A&A, 43, 133
Tennyson, J. 2005, Astronomical Spectroscopy: An Introduction to the Atomic and Molecular Physics of Astronomical Spectra (London: Imperial College Press)
Torres, G. 2010, AJ, 140/5, 1158
Unsold, A. 1974, Der neue Kosmos, 2nd edn. (Berlin Heidelberg: Springer)
Wisotzki et al. 1996, A&AS, 115, 227
Wisotzki et al. 2000, A&A, 358, 77

A Appendix

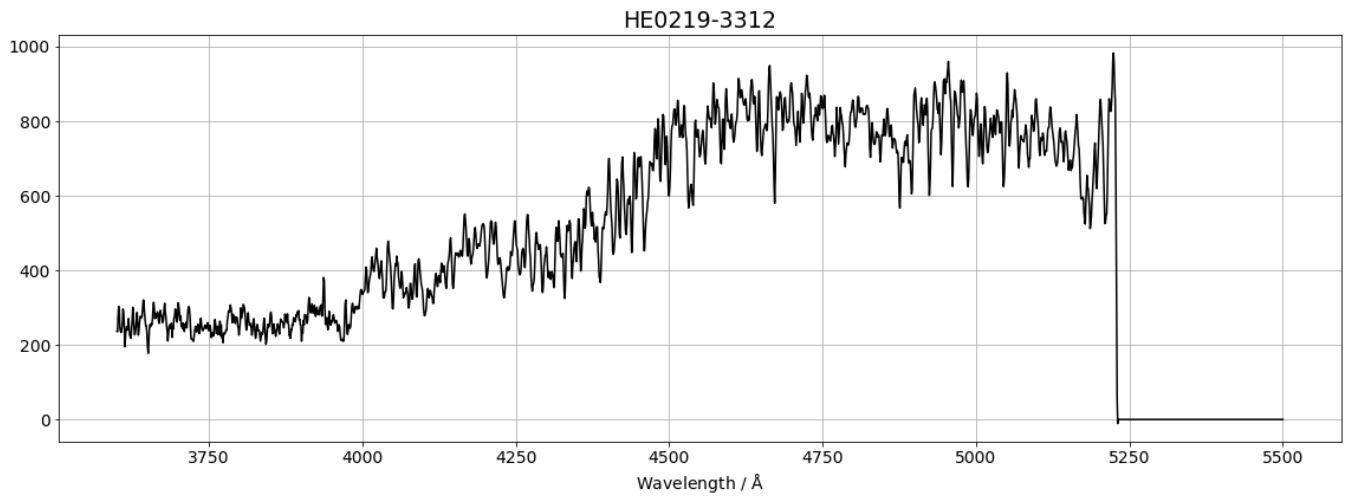
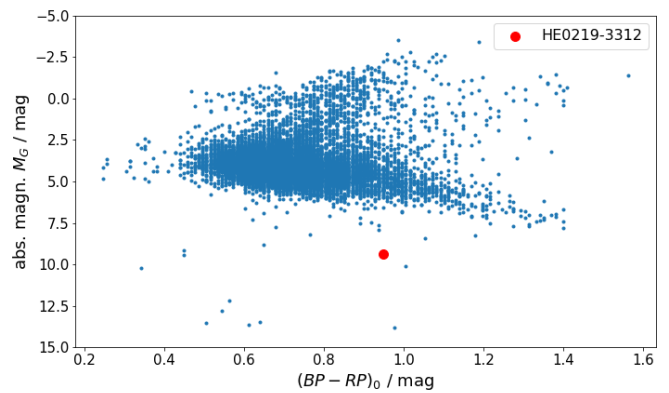
HE 0205-2434

Gaia DR2 source id: 5121507363836349312
 ra: 02 07 48.8
 dec: -24 20 06.4
 Distance: $1192.91^{+173.97}_{-136.41}$ pc
 Absolute G magnitude: 5.934 mag
 $(BP - RP)_0$ colour: 0.747 mag
 Effective temperature: $6084.3^{+271.5}_{-297.3}$ K



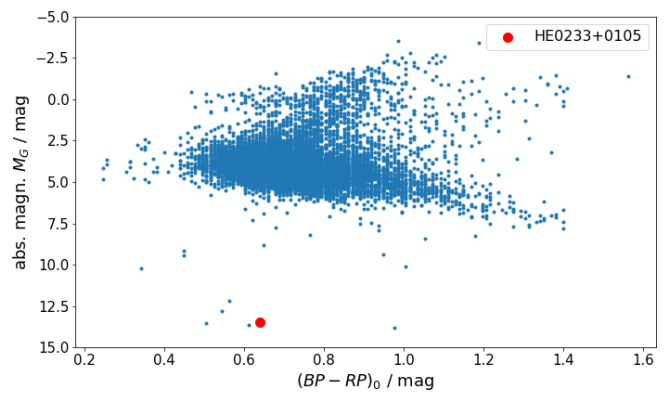
HE 0219-3312

Gaia DR2 source id: 4970501884284727680
 ra: 02 21 35.1
 dec: -32 58 37.1
 Distance: $133.32^{+0.59}_{-0.58}$ pc
 Absolute G magnitude: 9.357 mag
 $(BP - RP)_0$ colour: 0.948 mag
 Effective temperature: $4800.0^{+234.0}_{-101.3}$ K
 $[\text{Fe}/\text{H}]_{\text{K}} = -2.1$; $[\text{Fe}/\text{H}]_{\text{R}} = -2.6$; $[\text{C}/\text{Fe}]_{\text{R}} = 0.2$

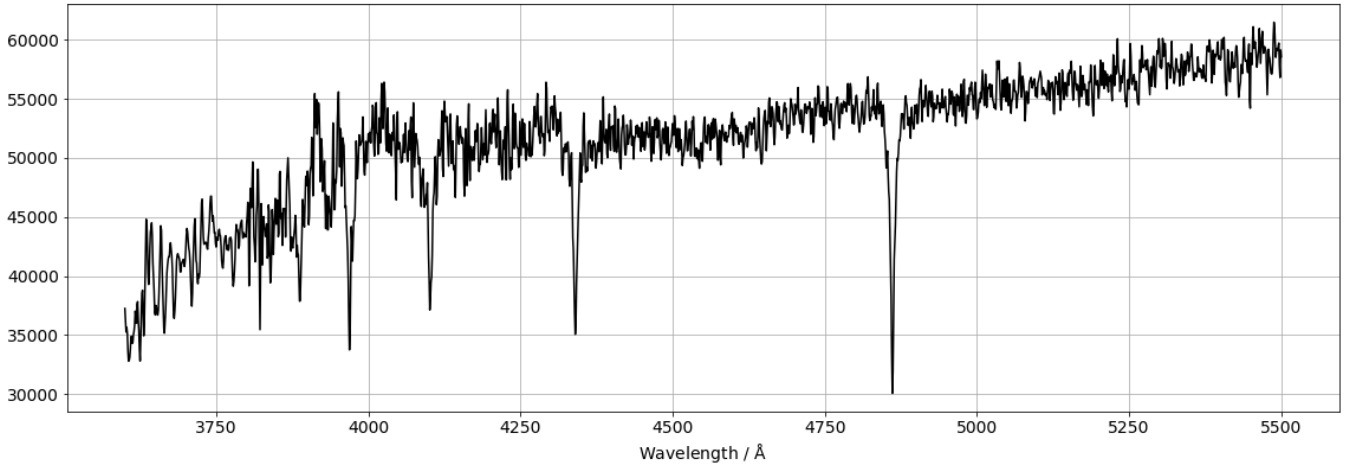


HE 0233+0105

Gaia DR2 source id: 2502097283492466560
 ra: 02 35 51.3
 dec: +01 18 44.9
 Distance: $33.04^{+0.07}_{-0.07}$ pc
 Absolute G magnitude: 13.492 mag
 $(BP - RP)_0$ colour: 0.641 mag
 Effective temperature: $6918.8^{+293.5}_{-240.8}$ K
 $[C/Fe]R = 4.6$

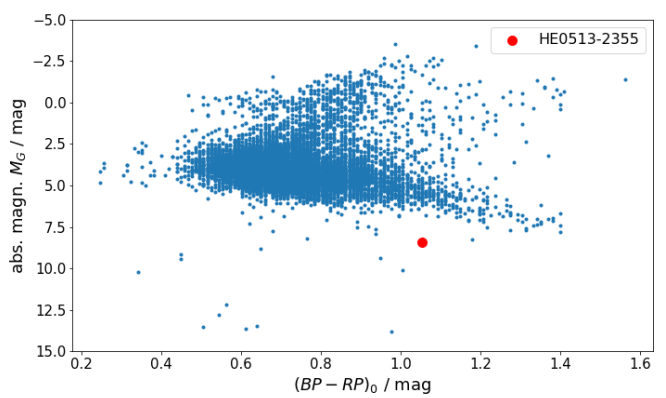


HE0233+0105

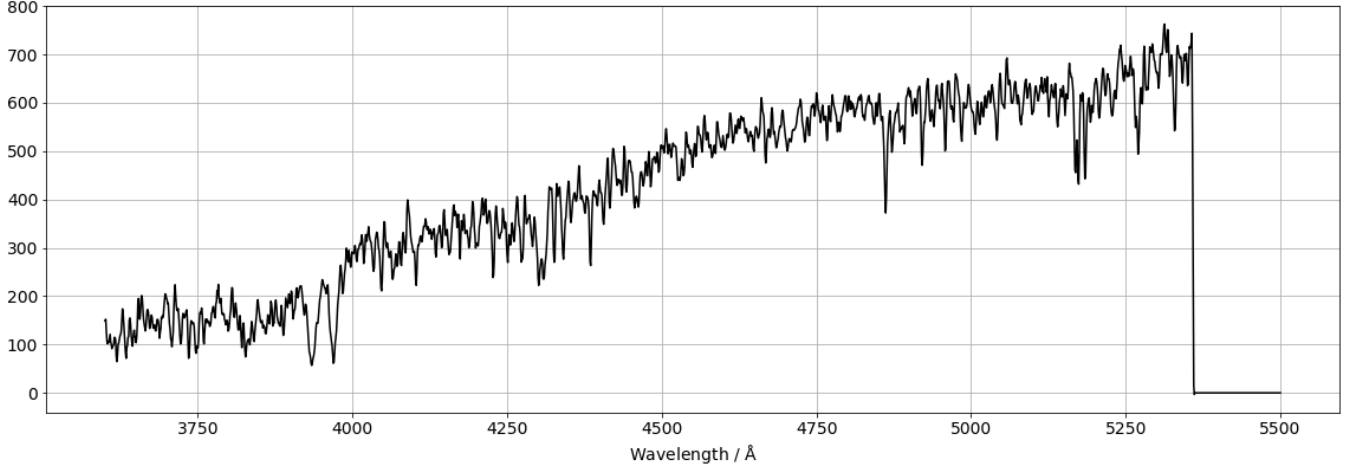


HE 0513-2355

Gaia DR2 source id: 2961177094994681472
 ra: 05 15 50.9
 dec: -23 52 39.4
 Distance: $221.22^{+43.27}_{-31.21}$ pc
 Absolute G magnitude: 8.409 mag
 $(BP - RP)_0$ colour: 1.054 mag
 Effective temperature: $5215.7^{+190.3}_{-550.2}$ K
 $[Fe/H]K = -2.7$; $[Fe/H]R = -1.8$; $[C/Fe]R = 0.8$

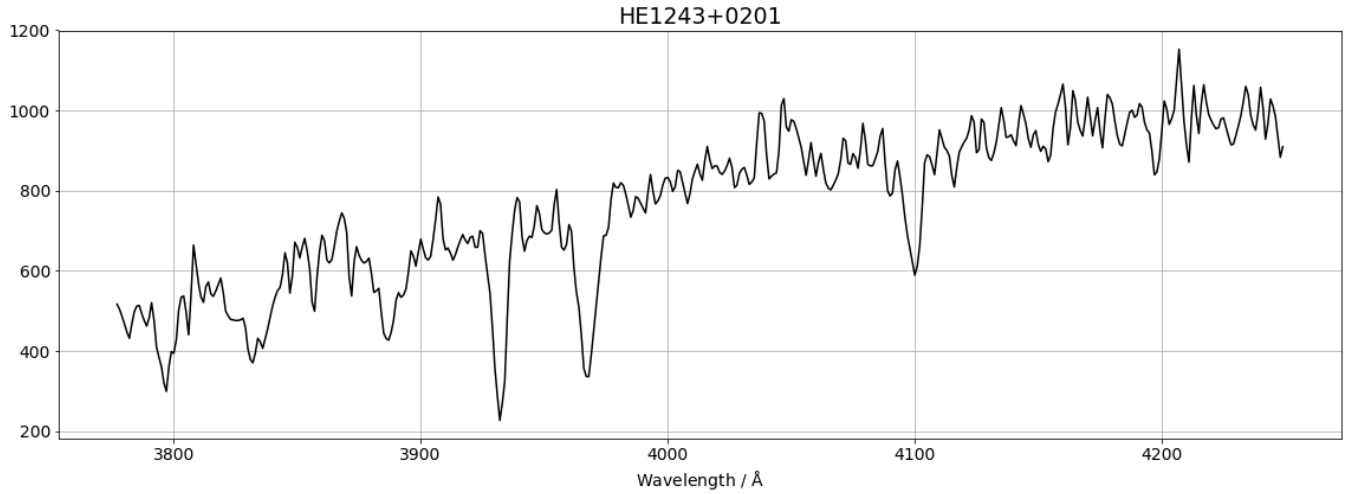
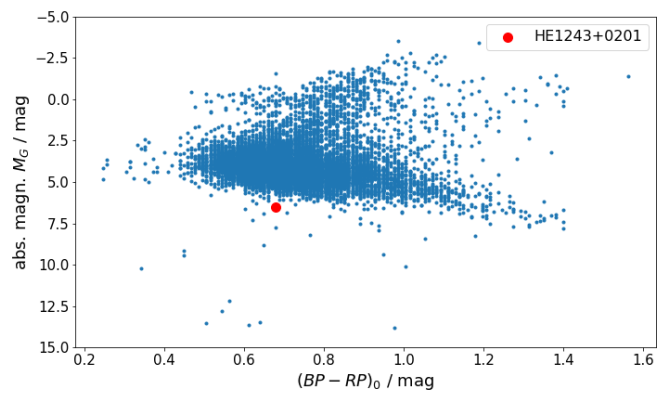


HE0513-2355



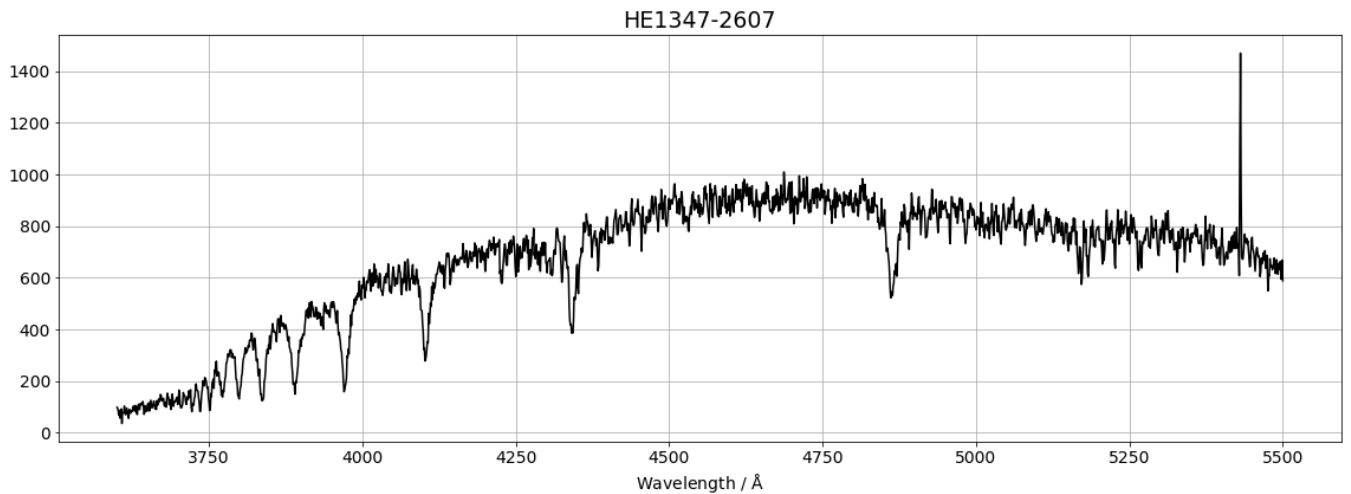
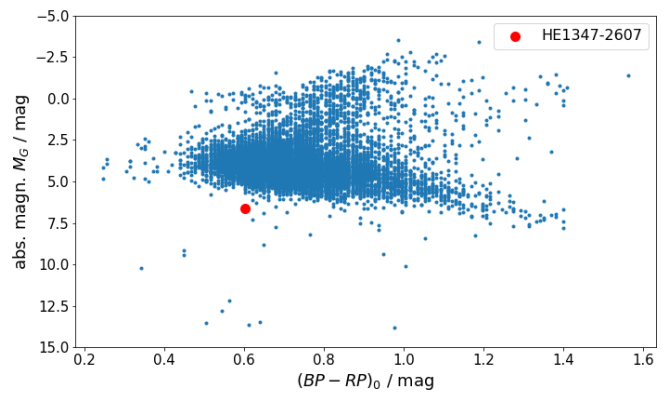
HE 1243+0201

Gaia DR2 source id: 3702435742443736448
 ra: 12 45 45.6
 dec: +01 45 22.6
 Distance: $565.64^{+72.24}_{-57.81}$ pc
 Absolute G magnitude: 6.540 mag
 $(BP - RP)_0$ colour: 0.679 mag
 Effective temperature: $6338.4^{+402.3}_{-319.1}$ K
 $[\text{Fe}/\text{H}]_{\text{K}} = -2.1$; $[\text{Fe}/\text{H}]_{\text{R}} = -2.8$; $[\text{C}/\text{Fe}]_{\text{R}} = 0.8$



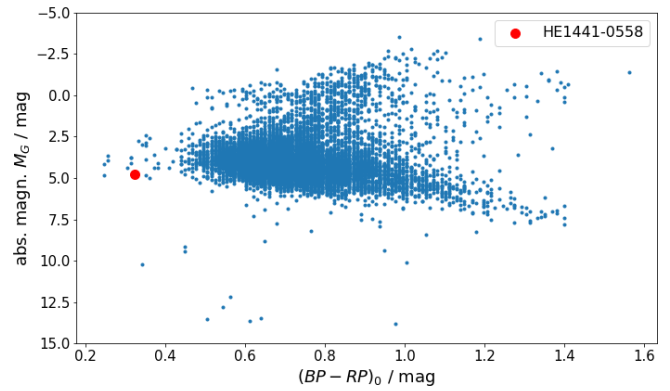
HE 1347-2607

Gaia DR2 source id: 6178664433616806656
 ra: 13 49 51.2
 dec: -26 22 48.3
 Distance: $356.64^{+92.37}_{-60.99}$ pc
 Absolute G magnitude: 6.628 mag
 $(BP - RP)_0$ colour: 0.603 mag
 Effective temperature: $5286.9^{+1763.1}_{-465.8}$ K
 $[\text{Fe}/\text{H}]_{\text{K}} = -0.7$; $[\text{Fe}/\text{H}]_{\text{R}} = -3.0$; $[\text{C}/\text{Fe}]_{\text{R}} = 0.6$

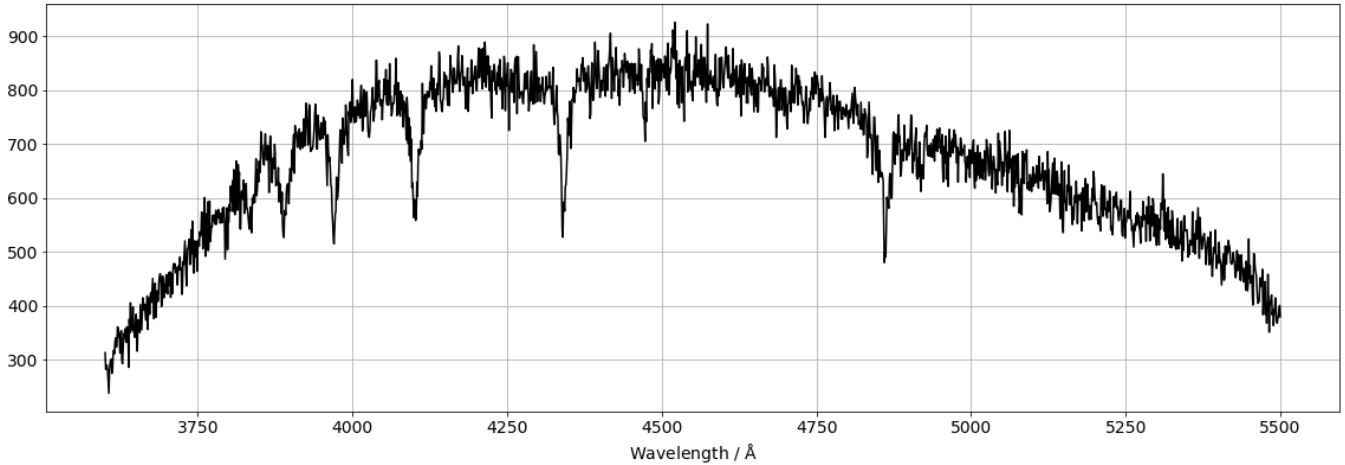


HE 1441-0558

Gaia DR2 source id: 6336921024852699648
 ra: 14 44 12.1
 dec: -06 10 44.8
 Distance: $729.87^{+23.68}_{-22.26}$ pc
 Absolute G magnitude: 4.791 mag
 $(BP - RP)_0$ colour: 0.324 mag
 Effective temperature: $9593.0^{+125.3}_{-1301.0}$ K
 $[C/Fe]R = 3.1$

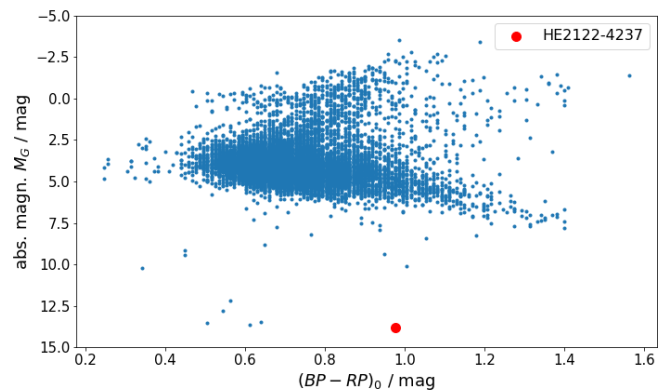


HE1441-0558

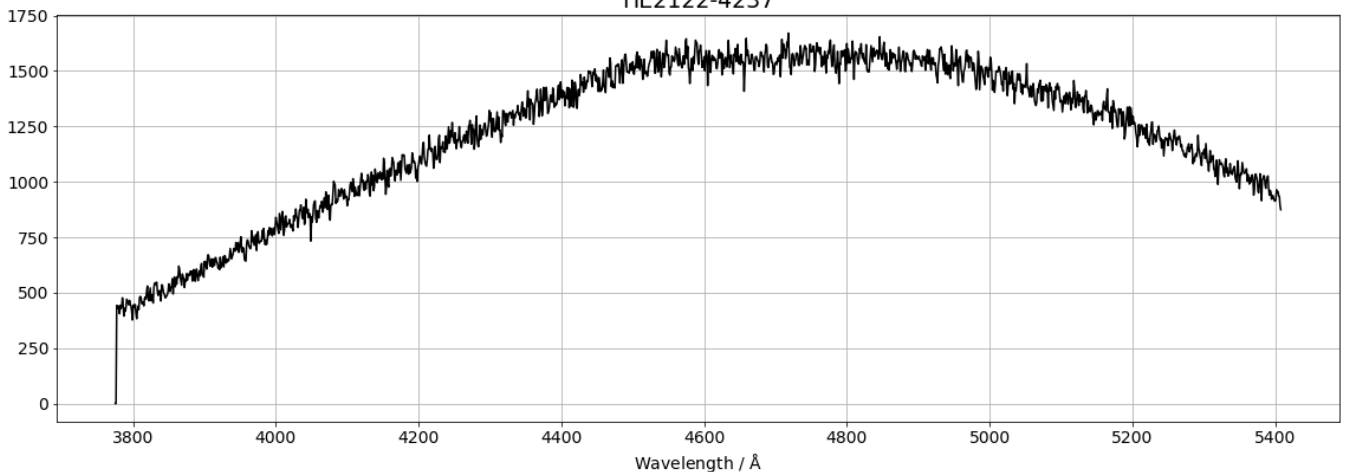


HE 2122-4237

Gaia DR2 source id: 6578917727331681536
 ra: 21 26 01.9
 dec: -42 24 52.8
 Distance: $23.6^{+0.17}_{-0.17}$ pc
 Absolute G magnitude: 13.816 mag
 $(BP - RP)_0$ colour: 0.977 mag
 Effective temperature: $5369.9^{+623.1}_{-453.8}$ K
 $[C/Fe]R = 2.7$

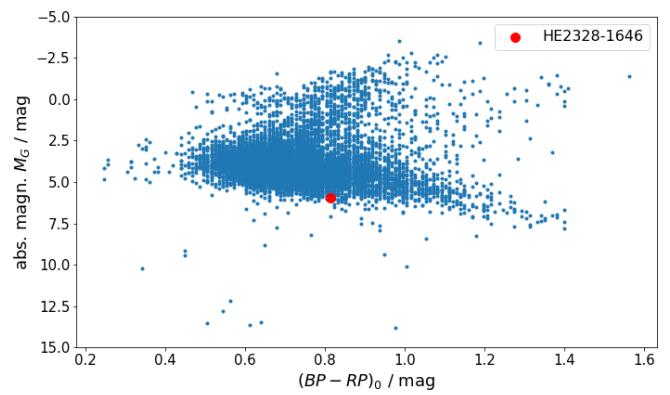


HE2122-4237

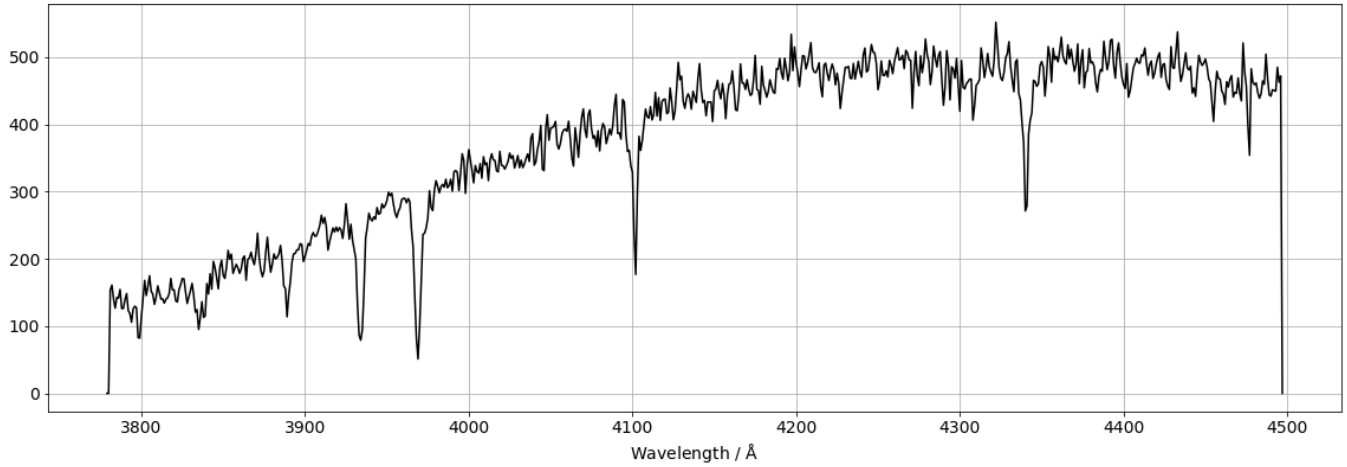


HE 2328-1646

Gaia DR2 source id: 2395285088973242496
 ra: 23 30 37.5
 dec: -16 29 56.9
 Distance: $1153.64^{+214.57}_{-158.8}$ pc
 Absolute G magnitude: 5.956 mag
 $(BP - RP)_0$ colour: 0.814 mag
 Effective temperature: $6178.8^{+624.4}_{-186.8}$ K
 $[C/Fe]R = -0.1$

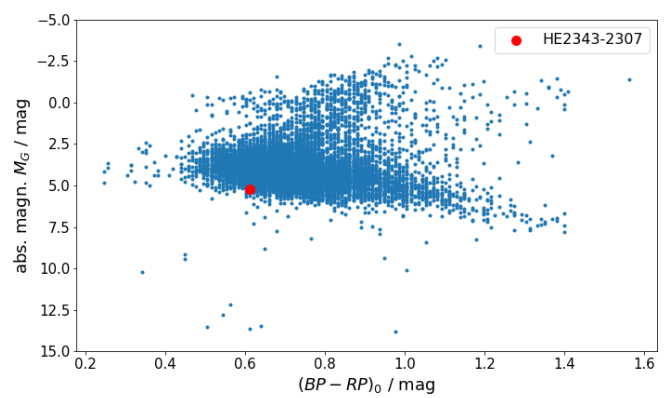


HE2328-1646

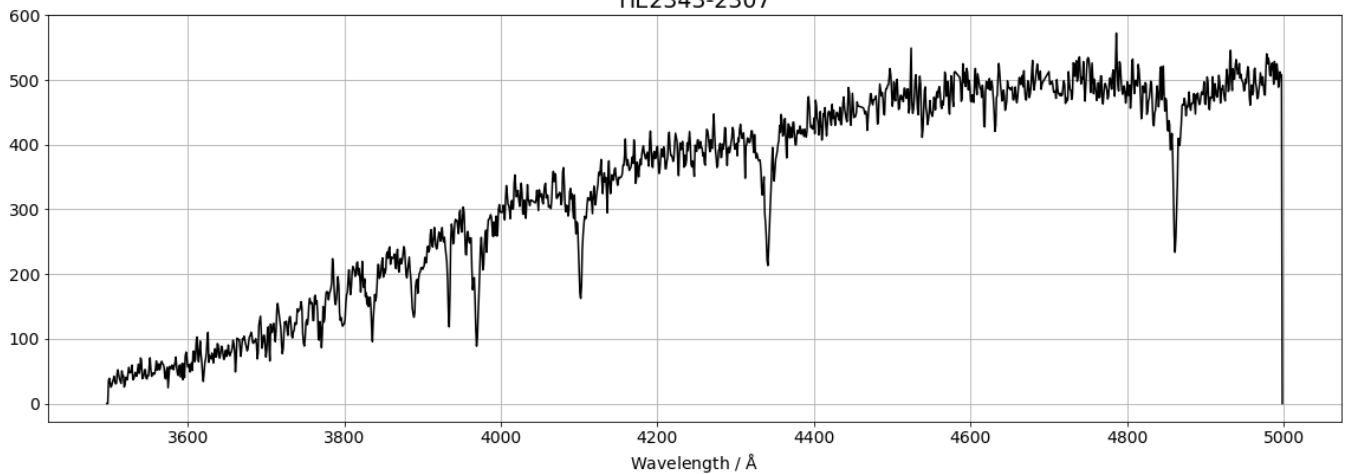


HE 2343-2307

Gaia DR2 source id: 2339473878747161600
 ra: 23 46 07.2
 dec: -22 50 38.2
 Distance: $1045.91^{+175.42}_{-132.94}$ pc
 Absolute G magnitude: 5.234 mag
 $(BP - RP)_0$ colour: 0.612 mag
 Effective temperature: $7302.0^{+595.8}_{-315.0}$ K



HE2343-2307



Erklärung

Ich versichere, dass ich diese Arbeit selbstständig verfasst und keine anderen als die angegebenen Quellen und Hilfsmittel benutzt habe.

Heidelberg, den 14.08.2020

Richter